Self-organized canals enable long range directed material transport in bacterial communities

Ye Li [1†], Shiqi Liu [1†], Yingdan Zhang [2], Zi Jing Seng [3], Haoran Xu [1], Liang Yang [2*], Yilin Wu [1*]

[1] *Department of Physics and Shenzhen Research Institute, The Chinese University of Hong Kong, Shatin, NT, Hong Kong, P.R. China.*

[2] *School of Medicine, Southern University of Science and Technology, Shenzhen, P.R. China.*

[3] *Singapore Center for Environmental Life Science Engineering, Nanyang Technological University, Singapore.*

†These authors contributed equally.

*Correspondence: Yilin Wu (ylwu@cuhk.edu.hk) and Liang Yang (yangl@sustech.edu.cn).

Abstract

Long-range material transport is essential to maintain the physiological functions of multicellular organisms such as animals and plants. By contrast, material transport in bacteria is often short-ranged and limited by diffusion. Here we report a unique form of actively regulated long-range directed material transport in structured bacterial communities. Using *Pseudomonas aeruginosa* colonies as a model system, we discover that a large-scale and temporally evolving open channel system spontaneously develops in the colony via shear-induced banding. Fluid flows in the open channels support high-speed (up to 450 μm/s) transport of cells and outer membrane vesicles over centimeters, and help to eradicate colonies of a competing species *Staphylococcus aureus*. The open channels are reminiscent of human-made canals for cargo transport, and the channel flows are driven by interfacial tension mediated by cell-secreted biosurfactants. The spatial-temporal dynamics of fluid flows in the open channels are qualitatively described by flow profile measurement and mathematical modeling. Our findings demonstrate that mechanochemical coupling between interfacial force and biosurfactant kinetics can coordinate large-scale material transport in primitive life forms, suggesting a new principle to engineer self-organized microbial communities.

Introduction

Long-range directed material transport is essential to maintain the physiological functions of multicellular organisms; it helps an organism to transport nutrients, metabolic wastes and signaling molecules, to translocate differentiated sub-populations through the body, and to maintain pH or temperature homeostasis. Long-range directed transport in multicellular organisms is primarily driven by pressure-induced advection and by coordinated cilia beating. For example, hydraulic pressure due to active pumping drives the circulation of body fluid in blood and lymph vessel systems of animals (Scallan, Zawieja, Castorena-Gonzalez, & Davis, 2016); transpiration and capillary pressure passively drive the water transport through vascular tissues of plants (Sack & Holbrook, 2006); and cilia beating of epithelial cells drives the cerebrospinal fluid flow in brain ventricles (Faubel, Westendorf, Bodenschatz, & Eichele, 2016) as well as mucus flow in the respiratory tract (Huang & Choma, 2015).

By contrast, material transport in bacterial world is often short-ranged and limited by diffusion (either passive diffusion due to thermal energy or active diffusion due to self-propulsion of motile cells (X.-L. Wu & Libchaber, 2000)). At the single cell level, diffusion governs nutrient uptake and sets a fundamental limit on the size of bacterial cells (Berg, 1993; Nelson, 2003; Schulz & Jorgensen, 2001). In bacterial communities, diffusion has been assumed to dominate material transport (Lavrentovich, Koschwanez, & Nelson, 2013; PIRT, 1967; Shao et al., 2017); long-range directed material transport is deemed unusual, despite the notion that bacterial communities resemble multicellular organisms in many aspects such as coordinated metabolism, communication, and division of labor (D. D. Lee, Prindle, Liu, & Süel, 2017; Parsek & Greenberg, 2005; Shapiro, 1998; van Gestel, Vlamakis, & Kolter, 2015). Like in animals and plants, any form of long-range directed material transport would undoubtedly bring profound effect to the development, structure, and stress response of bacterial communities. Intriguingly, a few examples of long-range directed transport in bacterial communities were reported in recent years. Among these examples, it was shown that long-range flows were driven by flagellar motility in sediment biofilms (Fenchel & Glud, 1998; Petroff & Libchaber, 2014) and in bacterial colonies (Y. Wu, Hosu, & Berg, 2011; Xu, Dauparas, Das, Lauga, & Wu, 2019), with a typical flow speed comparable to the swimming speed of individual cells; directed transport can also be driven by passive forces such as osmosis and evaporation-

induced pressure gradient (Wilking et al., 2013; Y. Wu & Berg, 2012), with a speed of ~0.1-10 μm/s. Nonetheless, these forms of directed material transport all appear to lack autonomous regulation at the community level; the transport is either passive (Wilking et al., 2013; Y. Wu & Berg, 2012) or driven by locally interacting cells (Fenchel & Glud, 1998; Petroff & Libchaber, 2014; Y. Wu et al., 2011; Xu et al., 2019). Intra-colony channel structures have been identified in a few bacterial species (Davey, Caiazza, & O'Toole, 2003; Drury, Characklis, & Stewart, 1993; Rooney, Amos, Hoskisson, & McConnell, 2020; Stoodley, DeBeer, & Lewandowski, 1994; Xu et al., 2019); these channel structures have a typical persistence length of a few micron to tens of microns, thus not able to support directed transport beyond millimeter scale.

Here we report a unique form of actively regulated long-range directed transport in structured bacterial communities. Using *Pseudomonas aeruginosa* colonies as a model system (Ramos, Dietrich, Price-Whelan, & Newman, 2010), we discovered that large-scale, time-evolving open channels spontaneously emerge in the colony; these centimeter-long channels with a free surface are referred to as “bacterial canals”. Fluid flows in the bacterial canals support high-speed (up to 450 μm/s) transport of cells and outer membrane vesicles over centimeters and help to eradicate colonies of a competing species *Staphylococcus aureus*. The canals presumably emerge via a complex-fluid phenomenon known as shear-induced banding (Divoux, Fardin, Manneville, & Lerouge, 2016; Olmsted, 2008). The typical speed of fluid transport in bacterial canals is one to two orders of magnitude higher than those in previously reported forms of bacterial long-range transport (Fenchel & Glud, 1998; Petroff & Libchaber, 2014; Wilking et al., 2013; Y. Wu et al., 2011; Xu et al., 2019). Gene knock-out and physiological experiments show that canal flows are driven by surface tension gradient mediated by the *P. aeruginosa*-produced biofurfactant rhamnolipids (Lang & Wullbrandt, 1999; Müller et al., 2012). Flow profile measurement and mathematical modeling that involves multiple transport processes and quorum-sensing (QS) regulation (Mukherjee & Bassler, 2019) together reveal the spatial-temporal dynamics of fluid flows in bacterial canals. Overall, our findings demonstrate that mechanochemical coupling between interfacial force and biosurfactant kinetics can coordinate large-scale material transport in primitive life forms, advancing the understanding on multicellular microbial behavior and suggesting a new principle to design macroscopic patterns and functions of synthetic microbial communities (Brenner, You, & Arnold, 2008; Chen, Kim, Hirning, Josić, & Bennett, 2015;

Kong, Meldgin, Collins, & Lu, 2018; Luo, Wang, Lu, Ouyang, & You, 2021; Miano, Liao, & Hasty, 2020).

Results

P. aeruginosa colonies establish large-scale open channels supporting directed fluid transport

We cultured *P. aeruginosa* PA14 colonies on M9DCAA agar plates (Methods). In the colonies of wildtype and *pilB*-knockout mutant (PA14 Δ*pilB*; denoted as nonpiliated mutant), we were intrigued to observe rapid cellular flows streaming through the interior of the colonies, while there was little collective directed motion on both sides of the streams (Movie S1). The streams were tens of microns in width and up to millimeters in length, but their courses were highly unstable presumably due to continuous disruption by cellular motion driven by flagellar motility. On the other hand, for PA14 mutants without flagellar motility, namely PA14 *flgK*::Tn5 Δ*pilA* (with both flagellar motility and type-IV-pilus mediated motility disabled; denoted by "non-motile *P. aeruginosa*") (Beaussart et al., 2014) and PA14 *flgK*::Tn5 (without flagellar motility but with functional type-IV-pilus mediated motility; denoted by "piliated *P. aeruginosa*") (K. Lee et al., 2011) (Methods), we observed by naked eyes that the colonies of both strains presented many low-cell-density valleys extending from colony center to the edge over centimeters with high directional persistence (Fig. 1A-D). Under the microscope we found that these remarkable, centimeter-long valleys were fluid-filled, free-surface channels (i.e. open channels) ~5-10 μm in height and tens to several hundred μm in width, in which cells carried by the fluid flow streamed rapidly at speeds up to hundreds of μm/s in coherent directions (Fig. 1E, Fig. S1A; Movie S2, S3). The fluid flow in channels on average went towards the colony edge and stopped abruptly at the very end (i.e. the tip) of a channel, disappearing into the dense layer of cells near the edge (Fig. S1B; Movie S4). The fluid flow was sensitive to water content in the air environment and it was easily disrupted by decrease of humidity. Cells translocating along the channels eventually settled in near the colony edge and they may contribute to colony expansion; however, channel formation does not necessarily coincide with colony expansion (e.g., see Movie S4).

Nearby channels could merge with each other while individual channels could split, resulting in a large-scale channel network across the entire colony (Fig. 1B,D). These large-scale open channels have a free upper surface and therefore, they are distinct from the pipe-like closed channels or conduits previously reported in bacterial colonies (Drury et al., 1993; Rooney et al., 2020; Stoodley et al., 1994; Xu et al., 2019). The open channels we found here are reminiscent of human-made canals for cargo transport, so we refer to these open channels as "bacterial canals".

Microscopically, the bacterial canals observed in non-motile (PA14 *flgK*::Tn5 Δ*pilA*) and piliated (PA14 *flgK*::Tn5) *P. aeruginosa* colonies is similar to the unstable streams observed in wildtype *P. aeruginosa* (PA14) and nonpiliated mutant (PA14 Δ*pilB*) colonies, but the former have more stable courses and are thus able to support sustained long-range directed fluid transport. For this reason, and to exclude any potential contribution of flagellar motility to material transport (Y. Wu et al., 2011; Xu et al., 2019), we focused on bacterial canals in this study. When the amount of surface water on agar plates was reduced by extended drying (Methods), the piliated *P. aeruginosa* (PA14 *flgK*::Tn5) colonies displayed a unique branching morphology presumably driven by fingering instability in the presence of surface tension gradient in the colony (Trinschek, John, & Thiele, 2018; Troian, Wu, & Safran, 1989) (Fig. 1F). Interestingly each branch was highly directed and hosted a single canal that ran through the entire branch (Fig. 1F, Movie S5; Fig. S1C, Movie S6). The emergence of canals in such branching colonies occurred robustly at ~8 hr (at 30 ºC) or ~15 hr (at room temperature) after inoculation. Since canals in the branching colonies advanced in a predictable manner without merging, hereinafter we systematically characterized canal development and manipulated this process using branching colonies of piliated *P. aeruginosa* (PA14 *flgK*::Tn5).

Canal development requires rhamnolipids and is driven by surface tension gradient

P. aeruginosa produces the well-characterized biofurfactant (i.e. surface active agents that reduce interfacial energy or surface tension (Chandler, 1987)) rhamnolipids (Lang & Wullbrandt, 1999; Müller et al., 2012). Since canal development does not require cell

178 motility, we hypothesized that surface tension gradient (i.e. Marangoni stress (de
179 Gennes, Brochard-Wyart, & Quere, 2003)) mediated by rhamnolipids provided the
180 driving force for fluid transport in canals; note that the canal flows cannot be driven by
181 osmotic pressure, because osmolarity gradients of cell products (hence the resultant
182 osmotic flows) must be directing towards the colony center. As *in situ* measurement of
183 rhamnolipid concentration or surface tension within colonies and canals is challenging,
184 to examine our hypothesis, we chose to knock out *rhlA* gene (encoding a
185 rhamnosyltransferase essential for the production of rhamnolipids (Ochsner, Fiechter, &
186 Reiser, 1994)) in pilated *P. aeruginosa* (Methods). We found that this rhamnolipid-
187 deficient mutant (PA14 *flgK*::Tn5 Δ*rhlA*) was unable to develop canals (Fig. 2A); also the
188 colony showed no sign of any mesoscale flows under the microscope. Next, to show
189 that Marangoni stress could drive canal formation, we established artificial surface
190 tension gradient in colonies by injecting an exogenous source of rhamnolipids via a
191 programmable syringe pump (Methods), and it restored canal formation in colonies of
192 the rhamnolipid-deficient mutant (Fig. 2B). We note that the artificial surface tension
193 gradient also promoted colony expansion (Fig. 2B), but again canal formation does not
194 necessarily coincide with colony expansion (see Movie S4 and its legend; also see
195 Discussion). On the other hand, to examine whether canal formation involves agar
196 degradation due to any potential agarase or hydrolase activities, we measured the
197 height profile of the colony and agar with laser scanning confocal microscopy (Methods).
198 We found that while the colony thickness above agar had an abrupt drop near canals,
199 the height of agar under canals and other regions of the colony was uniform and there
200 was no sign of agar degradation (Fig. S2). Taken together, these results show that canal
201 development requires rhamnolipids but not agar degradation, and they provide strong
202 evidence that fluid flows in canals are driven by rhamnolipids-mediated surface tension
203 gradient.
204
205 When we applied a counteracting surface tension gradient directing towards the colony
206 center by placing an agar patch containing surfactant TWEEN 20 (50 mg/mL, surface
207 tension ~4×10^{-2} N/m) ~1 cm in front of a colony branch, fluid flows in the canal
208 gradually ceased and the canal (but not the colony branch) slowly retracted (Movie S7;
209 Methods), suggesting that the driving force of canal flows is comparable in magnitude to
210 that provided by a surface tension gradient of ~10^3 mN·m^{-2}. Moreover, using a
211 previously developed fluorescence reporter P$_{rhlA}$-*gfp*(*ASV*) for rhamnolipids synthesis

(Yang et al., 2009) (GFP-ASV is a short-lived derivative of GFP and its fluorescence intensity reflects the current rate of biosynthesis (Andersen et al., 1998); Methods), we found that the *rhlA* promoter activity was azimuthally symmetric in early-stage colonies and the overall P_{rhlA}-*gfp*(*ASV*) fluorescence increased monotonically until canals emerged (Fig. 2C,D). The result shows that rhamnolipids in the colony center were continuously synthesized, thus generating a radial gradient of surface tension.

Flow profiles reveal shear-induced banding and surface tension distribution during canal development

The temporal dynamics of fluorescence reporter P_{rhlA}-*gfp*(*ASV*) described in Fig. 2D indicated continuous accumulation of rhamnolipids in the colony center, which would generate a radial surface tension gradient with azimuthal symmetry at the initial stage of canal development. It is then intriguing why rapid flows only emerge in certain regions of the colony (i.e. in canals), even though at the initial stage of canal development every part of the colony at the same distance to the colony center should experience similar Marangoni stress; for instance, canals had already emerged while the colony was still nearly symmetric at T=15 hr in Fig. 2C. Flow speed measurement by particle image velocimetry (PIV) analysis (Methods) in colonies before canals became visible to naked eyes revealed that the flow speed profile in regions with homogeneous cell density distribution displayed flow regimes with distinct shear rates (Fig. 3A,B; Movie S8; Methods). The course of those high-shear-rate domains were initially unstable (Fig. 3C, 0-24 min) and similar to the unstable streams observed in wildtype *P. aeruginosa* (PA14) and nonpiliated mutant (PA14 Δ*pilB*) colonies; as time went by, fluid flows in the high shear domains carried away cells in nearby areas, and the course got widened and gradually became fixed canals (Fig. 3C, 32-56 min; also see Movie S9). The presence of distinct flow regimes under presumably uniform shear stress (Fig. 3A,B) and the instability of flow courses (Fig. 3C) are hallmarks of shear-induced banding, a phenomenon often seen in complex fluids (Divoux et al., 2016; Olmsted, 2008; Ovarlez, Rodts, Chateau, & Coussot, 2009). These results suggest that canals emerge via the onset of shear-induced banding in the colony fluids (see more in Discussion).

After the onset of canals, due to the coupling of rhamnolipid transport, cellular transport and QS regulation of rhamnolipid synthesis (Lang & Wullbrandt, 1999; Müller et al.,

2012), rhamnolipid distribution or surface tension along the canals may vary in space and time, giving rise to a complex and dynamic profile of surface tension gradient that drives fluid flows in canals. To characterize the spatial distribution of surface tension gradient, we sought to measure the flow speed profile in canals because flow speed is linearly proportional to Marangoni stress. PIV analysis as performed in Fig. 3A can only yield the spatially-averaged collective speed, so we switched to local velocity measurement with fluid tracers. In order to avoid perturbing canal flows by introducing external fluid tracers, we took advantage of the fact that some cells being transported along the canals were well isolated from others and these isolated cells could be used as natural fluid tracers. We seeded the colony with a small proportion of GFP(ASV)-expressing cells (PA14 *flgK*::Tn5 P_{lasB}-*gfp(ASV)*; Methods), and measured the flow speed in canals by tracking the movement of these fluorescent cells. The speed of cells being transported by canals were too fast to resolve cellular positions in a single image frame, so we computed the time-averaged speed of cells based on the long-exposure-time trajectories of cells in order to reduce the error in speed measurement (Fig. 3D; Methods). The speed of these cells varied significantly along a canal cross-section; it peaked near the canal center and was attenuated near the canal boundaries. We found that the time-averaged peak cell speed near the center of canals was ~200 μm/s (with transient speeds up to 450 μm/s) (Fig. 3D), higher than other reported forms of bacterial long-range directed transport (Fenchel & Glud, 1998; Petroff & Libchaber, 2014; Wilking et al., 2013; Y. Wu et al., 2011; Xu et al., 2019) and most forms of active bacterial motility (Mitchell & Kogure, 2006). Note that the type-IV-pilus mediated motility did not contribute to the movement of these isolated cells being transported in canals, since type-IV-pilus mediated motility requires surface attachment and the resultant speed is only a few μm/s (Talà, Fineberg, Kukura, & Persat, 2019), so the movement of cells indeed followed fluid motion in canals. We further measured the peak flow speed at different locations of canals. As shown by the plateau in Fig. 3E, we found a high-flow-speed region spanning ~20 mm from the canal tip towards the colony center, and the flow speed diminished further towards the colony center. This result reveals the spatial distribution of Marangoni stress and suggests that the surface tension near the colony center has decreased to a steady-state level, presumably due to the saturated concentrations of rhamnolipids there.

Spatial-temporal dynamics of fluid transport in canals

Measuring the speed profile as shown in Fig. 3E along a typical ~3-cm long canal is challenging; it requires scanning over at least ~10 locations, with each location taking ~5 min and the entire measurement taking >~1 hr (Methods). The trade-off between the large spatial scale of canals (centimeters) and the microscopic nature of speed-profile measurement makes it even more difficult to measure the temporal evolution of canal flows in experiment, so we resorted to mathematical modeling for understanding the spatial-temporal dynamics of canal flows. First of all, we used finite-element simulation of Navier-Stokes equation in a simplified canal geometry (Fig. 4A; Methods) to estimate that the Marangoni stress in canals was on the order of ~1000 $mN \cdot m^{-2}$ in order to support a peak flow speed of ~400 μm/s. This magnitude roughly corresponds to the surface tension gradient established between a saturated source of rhamnolipids (surface tension ~30 mN/m; Fig. S3) and a surfactant-free region (surface tension ~70 mN/m; Fig. S3) over a distance of ~4 cm, which is consistent with the notion that the colony center has saturated concentrations of rhamnolipids as revealed in Fig. 3E.

We then built a model to describe the mechanochemical coupling between interfacial force and biosurfactant kinetics, which involve the transport processes of colony constituents (including rhamnolipids, cell mass, QS molecules and nutrients) and QS regulation of rhamnolipid synthesis (Fig. 4B,C; SI Text). Surface tension (γ) is a function of surface density (Γ) of rhamnolipids at the liquid-air interface:

$$\gamma(\Gamma) = \Pi_{max} exp(-A\Gamma^2 / \Gamma_c^{\ 2}) + \gamma_\infty , \qquad [1]$$

where γ_∞ is the surface tension of saturated rhamnolipid solution (at concentration ≫ CMC) measured by the pendant drop assay (de Gennes et al., 2003) (Fig. S3), Π_{max} is the difference in surface tension between pure water and the saturated rhamnolipid solution (corresponding to the maximal amount of surface tension decrease due to rhamnolipids), Γ_c is a characteristic surface density of rhamnolipids, and A is a parameter relating bulk rhamnolipid concentration to its steady-state surface density (SI Text). The parameters γ_∞, Π_{max} in Eq. [1] were obtained by fitting the experimental measurement of the surface tension of rhamnolipid solutions (Fig. S3; SI Text). We introduced dimensionless surface density (Γ_n) and bulk concentration of biosurfactant

313 (c_n) as $\Gamma_n = \Gamma / \Gamma_c$ and $c_n = c / c_s$, which are coupled through the following equations:

314

315 $$\frac{\partial c_n}{\partial t} = \nabla \cdot (D_c \nabla c_n) - (k c_n - k A \Gamma_n^{\,2}) + \frac{N}{K_N + N} \alpha_R \rho \frac{B^m}{K_B^m + B^m}, \quad [2]$$

316

317 $$\frac{\partial \Gamma_n}{\partial t} = \nabla \cdot (D_\Gamma \nabla \Gamma_n) - \nabla \cdot [\eta_\Gamma \Gamma_n \nabla \gamma(\Gamma_n)] + (k c_n - k A \Gamma_n^{\,2}). \quad [3]$$

318

319 Eq. 2 describes the variation of c_n due to three processes, namely biosurfactant
320 diffusion, biosurfactant exchange between the liquid-air interface and the bulk phase,
321 and biosurfactant production. The biosurfactant exchange between the two phases is a
322 key element in the model (SI Text); it was considered in the analysis of Marangoni flows
323 induced by depositing surfactants into a liquid (Hanyak, Sinz, & Darhuber, 2012; Roché
324 et al., 2014) but rarely in previous studies of the role of surface tension during colony
325 development. The biosurfactant production rate is controlled by nutrient concentration
326 (N), bacterial density (ρ), and QS signal (auto-inducer) concentration (B) (Cao et al.,
327 2016); N, B and ρ follow another set of differential equations (SI Text). Similarly, Eq. 3
328 describes the variation of Γ_n due to biosurfactant diffusion, advective transport of
329 biosurfactant by fluid flows, as well as biosurfactant exchange between the liquid-air
330 interface and the bulk phase; the advective transport term arises because biosurfactant
331 molecules associated with the liquid-air interface are carried along by fluid flows driven
332 by the surface tension gradient $\nabla\gamma$ (de Gennes et al., 2003). In Eq. 2-3, D_Γ, D_c, η_Γ, k,
333 K_N, α_R, K_B, and m are constant parameters. The details of model equations and
334 parameters are described in SI Text and Table S2.

335

336 As shown by the numerical simulation results based on the model, the distribution of
337 interface-associated surfactant displayed a saturated region near the colony center (Fig.
338 4D) (corresponding to the region with minimal surface tension in Fig. S4A), followed by a
339 biphasic decrease towards the spreading front of the colony (corresponding to the
340 increase of surface tension in Fig. S4A). The resultant surface tension gradient (and
341 therefore flow speed) was nearly zero near the colony center, which agrees with the
342 experimental result (Fig. 3E); further away from the center, it displayed a pronounced
343 plateau (i.e. ranging from the peak to knee of each curve at specific time points,

corresponding to the region with rapid canal flows) with modest inclination (Fig. 4E). These results are in qualitative agreement with the measured flow speed profile in canals (Fig. 3E), justifying our model and supporting the notion that canal flows are driven by rhamnolipids-mediated surface tension gradient; note that the modest slope from peak to knee shown in each curve of Fig. 4E was not apparent in Fig. 3E, as it could have been obscured by the large variation of flow speeds measured in experiments or by the low temporal resolution of measurement (scanning over the entire canal takes >~1hr, during which time the true flow speed profile must have shifted and the spatial variation would be smoothed out to certain extent). More importantly, our simulation results were able to reveal that the entire plateau moves away from colony center at a speed of ~1 mm/hr, with the width increasing gradually from ~20 mm to ~30 mm in 15 hr while the height decreasing by ~20% (Fig. 4E). Consequently the high-speed directed flows at a specific location in the canal can persist for ~20-30 hr. Taken together, these modeling results provide a qualitative picture how a colony maintains high-speed directed transport along canals for an extended range both in space and time.

Directed fluid flows transport outer membrane vesicles and help to eradicate competitor colonies

Finally we examined whether the canals have other physiological functions besides helping cellular populations to translocate over long distances. *P. aeruginosa* produces outer membrane vesicles (OMVs) to deliver pathogenic factors, antimicrobial compounds, intercellular signals, and public goods that either dissolve poorly or are prone to rapid dilution in the extracellular milieu (Bomberger et al., 2009; Mashburn & Whiteley, 2005; Schwechheimer & Kuehn, 2015). OMVs are slow in diffusion because their sizes are highly heterogeneous ranging from several tens to hundreds of nanometers. To examine whether directed fluid flows in canals can facilitate long-range transport of OMVs produced by *P. aeruginosa*, we isolated OMVs from bacterial culture by centrifugation, labeled them fluorescently, and loaded the OMV dispersion into a canal by microinjection (Methods). We found that these OMVs, having a mean size of ~150 nm (Fig. S5), were transported along the canal over centimeter distances (Fig. 5A-C) with a peak speed of >200 μm/s (Movie S10).

P. aeruginosa is a primary member of poly-species microbial communities found in lung infections of cystic fibrosis (CF) patients, and it may engage in competitive interactions with other species such as *Staphylococcus aureus* (Chew et al., 2018). To examine the potential function of canal flows on interspecies competition, we co-cultured colonies of piliated *P. aeruginosa* (PA14 *flgK*::Tn5) and *S. aureus* on agar plates (Methods). We used *S. aureus* cells harboring a plasmid with constitutive GFP expression (Toledo-Arana et al., 2005), so that the cell mass in *S. aureus* colonies can be quantified by GFP fluorescence during the interaction with *P. aeruginosa* (Methods). We found that *S. aureus* colonies irrigated by canal flows were quickly eradicated (Fig. 5D; Movie S11; Fig. S6), with <2% of the initial cell mass remaining after 60 min of contact with canal flows (Fig. 5E, curve labeled as “irrigated”). By contrast, *S. aureus* colonies that were in contact with *P. aeruginosa* colony but did not encounter canal flows retained ~40% of the initial cell mass after 60 min of contact (Fig. 5E, curve labeled as “non-irrigated”). These results demonstrated that fluid flows in canals help to eradicate competing bacterial species. We suggest that canal flows may increase the flux of *P. aeruginosa*-produced antimicrobial substances, such as quinolines encapsulated in OMVs with antibacterial activities against Gram-positive bacteria (Mashburn & Whiteley, 2005) and toxic compounds carried by rhamnolipid micelles (Gdaniec et al., 2022), and therefore enhance the efficiency of inhibiting competing bacterial species. It should be noted that *P. aeruginosa* produces a variety of anti-Staphylococcal compounds such as quinolines, pyocyanin and LasA protease (Hotterbeekx, Kumar-Singh, Goossens, & Malhotra-Kumar, 2017). While hydrophobic substances such as quinolines are poorly diffusible within the colony, those hydrophilic substances dissolvable in water readily diffuse within the agar substrate and their concentration in canals will fade out in a fraction of a second. In both cases, the anti-Staphylococcal substances cannot directly benefit from canal transport, unless they are adsorbed to or encapsulated by larger particles that are slow in diffusion, such as outer membrane vesicles (OMVs) and surfactant micelles ranging from tens to hundreds of nm in size. Therefore the rapid eradication of *S. aureus* colonies was most likely due to substances encapsulated in OMVs (Mashburn & Whiteley, 2005) and rhamnolipid micelles (Gdaniec et al., 2022) that were transported by canals.

Discussion

We have discovered that *P. aeruginosa* colonies develop a large-scale and temporally evolving free-surface open channel system, which supports high-speed (up to 450 μm/s) material transport over centimeters. The open channels, or "bacterial canals" are presumably driven by rhamnolipid-mediated surface tension gradient. They spontaneously emerge in the colony following the onset of shear-induced banding of colony fluids. Our findings present a unique form of long-range directed transport in structured bacterial communities.

Many bacterial species isolated to date synthesize biosurfactants (Ron & Rosenberg, 2001). In surface-associated bacterial communities where interfaces are prevalent (O'Toole & Wong, 2016; Persat et al., 2015), the inhomogeneous synthesis of biosurfactants often result in surface tension gradients (Marangoni stress). Marangoni stress was previously suggested to contribute to the expansion of bacterial colonies (Angelini, Roper, Kolter, Weitz, & Brenner, 2009; Du et al., 2012; Fauvart et al., 2012; Rhodeland, Hoeger, & Ursell, 2020; Trinschek et al., 2018). Our findings present a conceptual advance regarding the potential role of biosurfactant-empowered Marangoni stress: It can act as a spatiotemporally regulated driving force for active long-range directed material transport within structured bacterial communities. In this connection, we emphasize the difference between directed material transport within bacterial colonies and colony expansion. Colony expansion normally does not lead to directed transport of materials within the colony. For example, during swarming of wildtype *P. aeruginosa* facilitated by Marangoni stress, the colony expansion speed was ~1 μm/s (Fauvart et al., 2012), which is one order of magnitude slower than individual cells' random motion (tens of μm/s) and consequently, a cell or a passive tracer placed in the colony is expected to undergo diffusive motion with a small drift (Zuo & Wu, 2020) rather than directed transport. Moreover, directed material transport within a colony does not necessarily coincide with colony expansion, and the speed of the two processes could differ by orders of magnitude. For example, self-organized motile rings drive directed transport in sessile bacterial colonies that barely expand (Xu et al., 2019)). In our current study, cell mass transported by canals may contribute to colony expansion but this is not always the case (e.g., see Movie S4); more importantly, the speed of directed transport via canals occurring inside the colony is two orders of magnitude greater than

that of typical colony expansion (~200 μm/s versus ~2 mm/hr). Nonetheless, our work provides an new ingredient (i.e., long-range material transport driven by interfacial mechanics) that will complement existing models such as fingering instability (Trinschek et al., 2018) and colony-growth optimization (Luo et al., 2021) to explain and control pattern formation in expanding *P. aeruginosa* colonies.

Does canal transport play any role during the colonization of *P. aeruginosa* outside the laboratory? To answer this question we need to look back at the behavior of wildtype *P. aeruginosa* in our experiments. As noted earlier, wildtype *P. aeruginosa* colonies also displayed rapid streams within the colony but the streams did not turn into stable and persistent canals (Movie S1). The instability was presumably caused by continuous displacement of cells driven by flagellar motility. Flagellar motility weakens cell-cell adhesion and disrupts the course of high-shear flow regimes, thus preventing the high-shear flow regimes from further developing into more stable courses or canals. We suggest that under certain circumstances where *P. aeruginosa* cells tend to downregulate flagellar motility, such as in the airways of patients with cystic fibrosis (Luzar, Thomassen, & Montie, 1985; Mahenthiralingam, Campbell, & Speert, 1994; Wolfgang, Jyot, Goodman, Ramphal, & Lory, 2004), *P. aeruginosa* could develop canals for material transport in clinical or natural environments. Indeed, another flagellated and biosurfactant-producing bacteria *Serratia marcescens* is able to develop canal-like structures during swarming (Fig. S7), but such structures are only found at the center of the colony where most cells appear to be sessile.

The presence of distinct flow regimes and the instability of flow courses at the early stage of canal development (Fig. 3A,B) suggest that canals emerge via the onset of shear-induced banding in the colony fluids. This notion points to a novel biological function of shear-induced banding that often occurs in complex fluids such as polymer solutions, surfactant micellar solutions and colloidal suspensions (Divoux et al., 2016; Olmsted, 2008; Ovarlez et al., 2009). To further examine the conditions of shear banding in colony fluids, we measured the flow profiles of bacteria-rhamnolipids mixtures resembling the colony constituents in PDMS microfluidic channels subject to uniform shear stress. Under controlled flow conditions in PDMS microfluidic channels, we found that the cross-sectional flow velocity profile of a mixture of dense bacterial suspension (~$1.35X10^{10}$ cells/mL) and concentrated rhamnolipids [at 10 mg/mL, ~100 times critical

478 miceller concentration (CMC) (Zhao, Shi, Ma, Han, & Zhang, 2018)] was highly
479 asymmetric and signaled shear banding (Fig. S8, panel A); whereas the flow velocity
480 profile of pure cell suspension at the same density or of a mixture of rhamnolipids (10
481 mg/mL) and dense 1.1-μm microsphere suspension (~1.9×10^{10} particles/mL) was closer
482 to the parabolic profile characteristic of Newtonian fluids (Fig. S8, panel B,C). This result
483 suggests that the onset of shear banding in *P. aeruginosa* colonies preceding canal
484 formation requires the interaction between cells and rhamnolipids (most likely in the form
485 of micelles). The detailed biophysical mechanism of this requirement warrants further
486 investigation as a unique rheological behavior of bacterial active matter (Guo, Samanta,
487 Peng, Xu, & Cheng, 2018; Liu, Shankar, Marchetti, & Wu, 2021; Martinez et al., 2020).
488
489 As amphiphilic molecules with surface active properties evolved well before motility
490 mechanisms in the history of life, the mechanism of directed material transport we
491 uncovered here could have long been employed by microbial communities for the
492 transport of cellular mass and cargos in natural environments such as soils and plant
493 leaves. Canal transport helps translocating cellular populations or slowly-diffusing
494 chemical substances over long distances. This form of active material transport could
495 shape the population structure and mediate stress response of bacterial communities,
496 especially in structured environments with heterogeneous population or chemical
497 distribution. On the other hand, with the advance of synthetic biology, mechanochemical
498 coupling between interfacial force and biosurfactant kinetics (including the synthesis,
499 diffusion, and transport) could become a new strategy to design self-organization and
500 sensory functions in synthetic microbial communities (Brenner et al., 2008; Chen et al.,
501 2015; Kong et al., 2018; Miano et al., 2020). For instance, the mechanism could be
502 exploited to transport drugs and chemical effectors loaded in vesicles in order to control
503 the communication and behavior of synthetic bacterial communities.

Methods

Bacterial strains and plasmids

Bacterial strains. The following strains were used: wildtype *P. aeruginosa* PA14 (having both flagellar and type-IV pilus motilities), piliated *P. aeruginosa* (PA14 *flgK*::Tn5; without flagellar motility but retaining type-IV pilus motility), and nonpiliated *P. aeruginosa* (PA14 Δ*pilB*; without type-IV pilus motility but retaining flagellar motility), gifts from Roberto Kolter, Harvard University (K. Lee et al., 2011); non-motile *P. aeruginosa* (PA14 *flgK*::Tn5 Δ*pilA*; without either flagellar or type-IV pilus motility) (Beaussart et al., 2014), a gift from George A. O'Toole, Dartmouth College; *P. aeruginosa* deficient in rhamnolipid production (PA14 *flgK*::Tn5 Δ*rhlA*; see details of strain construction below); *Staphylococcus aureus* clinical strain isolate 15981 harboring a plasmid pSB2019-*gfp* that expresses GFP constitutively (Toledo-Arana et al., 2005); *Serratia marcescens* ATCC 274. Single-colony isolates were grown overnight (~ 13-14 hr) in 10 mL culture tubes (unless otherwise stated) with shaking in LB medium (1% Bacto tryptone, 0.5% yeast extract, 0.5% NaCl) at 30 °C to stationary phase. Overnight cultures were used for inoculating colonies on agar plates.

Strain construction. Primers used below are listed in Table S1. To construct the rhamnolipid deficient strain *P. aeruginosa* PA14 *flgK*::Tn5 Δ*rhlA*, upstream of the *rhlA* gene were amplified with 1-*rhlA*_UpF and 2-*rhlA*_UpR primers. Downstream of *rhlA* gene are amplified with 3-*rhlA*_DownF and 4-*rhlA*_DownR primers. The sequences of *rhlA* were obtained from *Pseudomonas* genome database (http://www.pseudomonas.com/). The PCR amplification was performed with Q5 High-Fidelity DNA Polymerase (NEB, USA). Using Gibson Assembly Master Mix (NEB, USA), the two purified flanking PCR fragments (Promega, USA) were assembled with BamHI and HindIII-digested PK18 (Gm^r) suicide vector. 10 µL of the assembled products was transformed to *Escherichia coli* DH5a competent cell by heat shock. Transformants were selected on 60 µg/mL Gm-infused LB Lennox agar plates and the insert size was verified by PCR with Pk18-F and Pk18-R primers using Taq Polymerase (Thermo Fisher, USA). A triparental mating was performed with PA14 *flgK*::Tn5 to generate PA14 *flgK*::Tn5 Δ*rhlA* gene deletion, through conjugation together with the aid of RK600 helper plasmid strain. ABTC agar containing 10% sucrose was used for SacB-based

538 counterselection. Mutants were confirmed by *rhlA*_F and *rhlA*_R primers with PAO1
539 gDNA as a control. *rhlA*GENE_F and *rhlA*GENE_R primers were used to check for the
540 presence of *rhlA* gene with PAO1 gDNA as a control.
541
542 **Plasmids**. The rhamnolipid synthesis reporter plasmid pMHRA contains an RlhR-
543 regulated P_{rhlA}-*gfp(ASV)* fusion inserted into the vector pMH391 (Yang et al., 2009). *rhlA*
544 encodes a rhamnosyltransferase essential for the production of rhamnolipid under the
545 control of *rhl* QS system (Ochsner et al., 1994), and is thus a good indicator of *rhl* activity
546 (Yang et al., 2009). GFP-ASV is a short-lived derivative of GFP, which degrades with a
547 half-life < 1 h and is rapidly cleared from cells, thus its fluorescence intensity reflects the
548 current rate of biosynthesis (Andersen et al., 1998). For flow speed measurement in
549 canals, the plasmid pMHLB containing a translational fusion of the P_{lasB}-*gfp*(ASV) was
550 used (Hentzer et al., 2002); *lasB* encodes a virulence factor elastase under the control of
551 LasR (Hentzer et al., 2002) and is homogeneously expressed in the colony with
552 sufficiently bright fluorescence suitable for our tracking method. The plasmids were
553 introduced into PA14 *flgK*::Tn5 by electroporation. The transformants were selected on
554 LB 1.5% agar plates supplemented with gentamicin (50 µg/mL). These plasmids have
555 high copy numbers, so we did not need to add any antibiotics into culture environment to
556 prevent plasmid loss.
557
558
559 **Preparation of agar plates for colony growth**
560
561 *P. aeruginosa* colonies were grown on 0.5% Difco Bacto agar plates infused with
562 M9DCAA medium (Tremblay & Déziel, 2010)[20 mM NH_4Cl, 12 mM Na_2HPO_4, 22 mM
563 KH_2PO_4, 8.6 mM NaCl, 1mM $MgSO_4$, 1mM $CaCl_2$, 11 mM dextrose, and 0.5% (wt/vol)
564 casamino acids (BD Bacto, cat. No. 223050)]. We varied the agar concentration and
565 found that canals develop robustly over a relatively wide range of agar concentration
566 between 0.5% and 1.0% wt/vol (Fig. S9). Above 1.0%, canals were not observed
567 presumably because the cells have difficulty to extract sufficient water to maintain an
568 open-surface liquid film on the agar surface, which is the same underlying reason why
569 most bacteria cannot swarm on agar above 1.0% as swarming also requires maintaining
570 open-surface liquid films (Kearns, 2010). As Ca^{2+} cannot coexist stably with many ions,
571 this medium was prepared and stored in two components: (1) 10X nutrient solution

without $CaCl_2$, sterilized and stored at room temperature; (2) agar infused with $CaCl_2$ at $1\frac{1}{9}$ times of the desired concentrations, sterilized and stored in 100 mL aliquots. Before use, the component (2) was melted completely in a microwave oven and cooled to ~60 °C. For each plate, 18 mL molten component (2) was mixed with 2 mL component (1) and the mixture was poured to a polystyrene petri dish (90 mm diameter, 15 mm height). To quantify cell mass in the colony, the membrane dye FM 4-64 (Thermo Fisher Scientific) was added into the agar plates at a final concentration of 1 μg/mL. The plate was swirled gently to ensure surface flatness, and then cooled for 10 min without a lid inside a large Plexiglas (PMMA) box, followed by further drying under laminar airflow for 5 min or 20 min (to culture branching colonies). 1 μL overnight culture was used to inoculate colonies at the center of each plate, and the plates were incubated at specified temperatures and >~95% relative humidity; lowering the humidity will lower the probability of canal formation. The colonies expanded at a steady-state speed of ~2 mm/hr at 30 ºC. The emergence of canals in branching colonies of piliated *P. aeruginosa* (PA14 *flgK*::Tn5) occurred robustly at ~8 hr (at 30 ºC) or ~15 hr (at room temperature) after inoculation. In experiments co-culturing *P. aeruginosa* and *S. aureus*, half of casamino acids in the M9DCAA medium described above was replaced by peptone at a final concentration of 0.25% (wt/vol) in order to support growth of *S. aureus*; this medium was referred to as M9DCAAP. The M9DCAAP plates were prepared following the same procedures as described above and incubated at 30 ºC and >~95% relative humidity.

Imaging colonies and canals

The macroscale dynamics of *P. aeruginosa* colony or canal development was monitored and measured in a custom-built imaging incubator made of PMMA (l × d × h, 1 × 1 × 1.2 m). The agar plates were sealed with parafilm before incubation in order to maintain saturated humidity. The temperature of the incubator was maintained at 30 °C with a heater controlled by feedback circuits. The inner walls of the incubator were covered with black cloth and the plate was illuminated by an LED strip lining at the bottom part of the side walls. The images of colonies or canals were photographed by a digital single-lens reflex camera (DSLR; Canon 700d) every 5 min during incubation (24 mm for whole plate view or 60 mm for zoomed-in view, aperture f/8, exposure time 1/5 s). The time-lapse imaging and LED illumination were triggered by a custom-programmed

606 microcontroller (Arduino). Phase-contrast microscopy imaging of canal development
607 was performed on an inverted microscope (Nikon TI-E) via a 10X dark phase objective
608 (N.A. 0.25) or a 4X dark phase objective (N.A. 0.13). Recordings were made with an
609 sCMOS camera (Andor Zyla 4.2 PLUS USB 3.0; Andor Technology) or the DSLR
610 camera (Canon 700d; triggered by a custom-programmed Arduino microcontroller).
611
612 **Height profile measurement of the colony and agar with laser scanning confocal**
613 **microscopy**
614
615 Molten M9DCAA 0.6% agar was mixed with 0.5 µm-diameter fluorescent microsphere
616 (FluoSpheres carboxylate-modified, ex/em: 580 nm /605 nm; Thermofisher F8812) at a
617 final microsphere number density of 3.1 $x10^{11}$ particles/mL (~1000-fold dilution of the
618 microsphere solution). 20 mL of the agar-microsphere mixture was poured into a 60-mm
619 diameter petri dish. After the agar solidified, the plate was dried under laminar flow
620 without the lid for 30 min. 1 µL overnight culture of *P. aeruginosa* PA14 *flgK*::Tn5
621 harboring the pMHLB plasmid [with P_{lasB}-*gfp*(ASV), as described above] was inoculated
622 into the center of the agar plate. The plate was then sealed by parafilm and incubated in
623 a 30 ºC incubator without humidity control for ~24 hr before observation. The 3D
624 structures of the agar and the bacterial colony near canals were imaged with a Leica
625 SP8 laser scanning confocal microscope via a 10X objective (N.A. 0.30). Green
626 fluorescence acquired from cells in the colony (excitation: 476 nm, emission: 480-550
627 nm) and red fluorescence from the microspheres homogeneously dispersed in agar
628 (excitation: 562 nm, emission: 588-658 nm) provided spatial information of the colony
629 and the agar, respectively. The thickness of optical section was set as 12.85 µm. A total
630 of 71 frames at different vertical positions with an interval of 4.28 µm were scanned to
631 acquire the 3D structures. To compute the height profiles of the colony and the agar, we
632 first obtained the 2D cross-sectional fluorescence intensity distributions in both green
633 and red channels by averaging the 3D fluorescence image over the thickness of the
634 optical section. We then binarized the 2D fluorescence intensity distributions in both
635 channels to determine the boundaries of the colony and the agar, thus obtaining the
636 thickness of the colony and the height profile the agar underneath the colony.
637
638 **Establishing exogenous surface tension gradients**
639

Rhamnolipid solution (10 mg/mL) was injected into the colony center of the rhamnolipid-deficient mutant *P. aeruginosa* PA14 *flgK*::Tn5 Δ*rhlA*, in order to create a surface tension gradient pointing radially outwards. To inject exogenous rhamnolipid solutions into the colony, one microliter of PA14 *flgK*::Tn5 Δ*rhlA* overnight culture was inoculated at the center of an M9DCAA agar plate, and the plate was incubated for 20 hr at room temperature and >~95% relative humidity. Then the lid was replaced by one with a drilled hole, and 10 mg/mL rhamnolipid solution (rhamnolipids 90%, in solid form, AGAE Technologies; dissolved in M9DCAA medium) loaded in a 100 µL glass microsyringe (W-018107, Shanghai Gauge) was pumped into the center of the colony at the rate of 5 µL/hr by a syringe pump (Fussion 200, Chemyx) via a PTFE tube (inner diameter 0.3 mm) that passed through the hole in the lid. The chosen rhamnolipid concentration [10 mg/mL, ~100 times critical miceller concentration (CMC) (Zhao et al., 2018)] was on the order of maximal rhamnolipid concentration that can be produced by *P. aeruginosa* (Soares Dos Santos, Pereira, & Freire, 2016). The end of the PTFE tube barely touched the upper surface of the colony surface. Images of the colony were taken with a DSLR camera (Canon 700d).

To apply a counteracting surface tension gradient directing towards the colony center, we placed an agar patch containing surfactant TWEEN 20 (50 mg/mL) in front of a colony branch. To prepare the surfactant-infused agar patches, we supplemented the surfactant Tween 20 (Sigma) to molten M9DCAA 3% agar at a final concentration 50 mg/mL, poured 10 mL of this agar into 90 mm petri dishes, and cut out 10 mm x 5 mm rectangular patches after the agar solidified. We placed a piece of the surfactant-infused agar patch at ~1 cm in front of a branch of a *P. aeruginosa* PA14 *flgK*::Tn5 colony that had grown for 20 hr at 30 ºC. Immediately following the placement of the agar patch, the agar plate was transferred to the stage of an inverted microscope (Nikon Ti-E) and the colony branch was observed via a 4X dark phase objective (N.A. 0.13). Image recordings were made with an sCMOS camera (Andor Zyla 4.2 PLUS USB 3.0; Andor Technology). Control experiments followed the same procedures, except that TWEEN 20 solution was replaced by M9DCAA medium when preparing the agar patch.

Fluorescence imaging of rhamnolipid synthesis reporter and data processing

We measured the synthesis level of rhamnolipids during the early stage of canal

development using a fluorescence reporter P_{rhlA}-*gfp*(*ASV*) for the promoter activity of *rhlA* gene as described above. One microliter of the overnight culture of *P. aeruginosa* PA14 *flgK*::Tn5 hosting the plasmid P_{rhlA}-*gfp(ASV)* was inoculated at the center of an M9DCAA agar plate, and the plate was incubated in a sealed glass box with four beakers (each containing 5 mL DI water) at the corners to maintain saturated humidity. The glass box was then transferred to the motorized stage (HLD117, PRIOR Scientific Instruments) on an inverted microscope (Nikon Ti-E) for imaging at room temperature. Multichannel fluorescent images were acquired with a 4X objective (N.A. 0.13) and an FITC/Texas Red dual-band filter set (excitation: 468/34 nm and 553/24 nm, emission: 512/23 nm and 630/91 nm, dichroic: 493 to ~530 nm and 574 to ~700 nm; Semrock, cat. No. GFP/DsRed-A-000) with the excitation light provided by a high-power LED light source (X-Cite XLED1, Excelitas Technologies Corp.). For excitation of GFP, BDX LED lamp module (450-495 nm) was turned on and the exposure time was set as 500 ms. For FM 4-64 excitation, GYX module (540-600 nm) was turned on and the exposure time was set as 5 s. The imaging protocol was executed by a custom-programmed microcontroller (Arduino) through the software NIS Element AR (v 4.51, Nikon). Images were recorded with an sCMOS camera (Andor Zyla 4.2 PLUS USB 3.0; Andor Technology).

The overall fluorescence count of P_{rhlA}-*gfp(ASV)* reporter and FM 4-64 at the colony center was computed by integrating the fluorescence intensity over the entire inoculum region. For each image stack, the image with the lowest overall fluorescence count was chosen as the background and subtracted from the rest of images in the stack. Different colonies may have different lag times due to slight variation of inoculum size across experiments, but their growth dynamics after the lag time is highly conserved.

Measurement of shear banding

To observe shear banding in colonies, *P. aeruginosa* PA14 *flgK*::Tn5 hosting the plasmid P_{rhlA}-*gfp(ASV)* was inoculated as described above. To observe shear banding in PDMS microfluidic channels, *P. aeruginosa* PA14 *flgK*::Tn5 was grown in 250 mL glass flasks with shaking in LB medium (1% Bacto tryptone, 0.5% yeast extract, 0.5% NaCl) at 30 °C to a cell density ~2.1 X 10^9 cells/mL, and the culture was concentrated to ~2.1X10^{10} cells/mL and resuspended in M9DCAA medium before use. PDMS chips with

708 microfluidic channel was fabricated by standard soft lithography technique (Whitesides,
709 Ostuni, Takayama, Jiang, & Ingber, 2001) and sealed to cleaned glass coverslip. The
710 cross-section of microfluidic channels was rectangular, 1.1 mm in width, 200 μm in
711 height, and 4 cm in length. Fluids (~200 μL) were loaded into a glass syringe and
712 pumped into the microfluidic channels by the syringe pump (Chemyx Fusion 200, Two-
713 channel Syringe Pump Model 07200) via a polytetrafluoroethylene (PTFE) tube (inner
714 diameter 0.41 mm, outer diameter 0.92 mm). Before loading the fluids of interest, fresh
715 M9DCAA medium was preloaded into the channel. For experiments with cell-
716 rhamnolipid mixtures, the concentrated bacterial culture (~$2.1X10^{10}$ cells/mL
717 resuspended in M9DCAA medium) was mixed with rhamnolipid stock solution (100
718 mg/mL) at 9:1 ratio (final concentration of rhamnolipids: 10 mg/mL, ~100 times CMC;
719 final cell density: ~$1.9X10^{10}$ cells/mL) and injected into the microfluidic channel for
720 observation. For experiments with microsphere-rhamnolipid mixtures, microsphere
721 dispersion (Polybead sulfate, 1.1 μm diameter, Polyscience Inc.) was mixed with
722 rhamnolipid (final concentration of rhamnolipids: 10 mg/mL; final number density of
723 microspheres: ~$1.9x10^{10}$ particles/mL). The flow rate was maintained constant during
724 observation, ranging from 3 μL/min to 5 μL/min.
725
726 The observations were performed on an inverted phase-contrast microscope (Nikon TI-
727 E). Shear banding in colonies was observed with a 20X objective (N.A. 0.45, w.d. 8.2–
728 6.9 mm; Nikon, MRH48230) and experiments in PDMS microfluidic channels was
729 imaged with a 10X objective (N. A. 0.25, w.d. 6.2mm; Nikon). Videos were recorded with
730 an sCMOS camera (Andor Zyla 4.2 PLUS USB 3.0; Andor Technology) at 50fps.
731 Velocity field was computed by performing PIV analysis on phase contrast microscopy
732 image sequences using an open-source package MatPIV 1.6.1 written by J. Kristian
733 Sveen (https://www.mn.uio.no/math/english/people/aca/jks/matpiv/). For each pair of
734 consecutive images, the interrogation-window size started at 41.6 μm × 41.6 μm and
735 ended at 10.4 μm × 10.4 μm after four iterations. The grid size of the resulting velocity
736 field was 5.2 μm × 5.2 μm.
737
738
739 **Measurement of flow speed in canals**
740

741 In order to avoid perturbing canal flows by introducing external fluid tracers, we used
742 fluorescent cells being transported by canal flows as natural fluid tracers. Note that the
743 type-IV-pilus motility did not contribute to the movement of these cells, since type-IV-
744 pilus motility requires surface attachment and the resultant speed is only a few μm/s
745 (Talà et al., 2019). The overnight culture of *P. aeruginosa* PA14 *flgK*::Tn5 harboring the
746 pMHLB plasmid [with P_{lasB}-*gfp*(ASV), as described above], whose GFP(ASV) expression
747 was sufficiently bright and uniform along canals for tracking purposes, was mixed with
748 the overnight culture of PA14 *flgK*::Tn5 at a ratio of 1:100. One microliter of this mixture
749 was inoculated at the center of an M9DCAA agar plate, and the plate was incubated for
750 20 hr at 30 ºC and >~95% relative humidity. The fluorescent bacteria were imaged on
751 an upright microscope (ECLIPSE Ni-E; Nikon) via a 40X objective (N.A. 0.75) and a
752 FITC filter cube (excitation: 482/35 nm, emission: 536/40 nm, dichroic: 506 nm long pass
753 filter; FITC-3540C-000, Semrock Inc.), with the excitation light provided by a mercury
754 precentered fiber illuminator (Intensilight, Nikon), and recordings were made with an
755 sCMOS camera (Andor Neo 5.5; Andor Technology).
756
757 Due to the ultrahigh speed (up to hundreds μm/s) of cells, resolving the position of
758 tracers (cells) frame by frame requires a very short exposure time (<~10 ms) per frame,
759 but such a short exposure time could not yield sufficient photon count to distinguish cells
760 from the background. To overcome this difficulty we recorded cell trajectories during a
761 long exposure time (0.5~5 s) (Fig. 3D), and computed the average speed of cells during
762 the exposure time. This way allowed us to reduce the error in speed measurement due
763 the ultrafast movement of cells. 50 such recordings were made at each position of the
764 canal to yield sufficient number of cell trajectories. All recordings at a specific position
765 were completed within 5 min from placing the agar plate on microscope stage in order to
766 minimize the effect of evaporation. The images were imported into MATLAB (R2014b,
767 The MathWorks; Natick, Massachusetts, United States). For each trajectory, five points
768 (including the two ends) were selected manually using datacursormode function in
769 MATLAB user interface. The selected points were fitted by quadratic spline interpolation
770 (splineinterp function in MATLAB Curve Fitting Toolbox). The length of the fitted curve
771 was taken as the length of the trajectory, and the average speed of the cell was then
772 calculated as the trajectory length divided by the exposure time. In each measurement,
773 the position of field of view relative to the canal tip was determined by moving the
774 motorized stage of the microscope, with an uncertainty of ~1 mm.

775

776 **Numerical simulation of flows in a simplified 3D canal geometry**

777

778 To estimate the magnitude of surface tension gradient driving flows in canals, we
779 performed a finite-element simulation of Navier-Stokes equation in a simplified 3D canal
780 geometry using the software COMSOL Multiphysics (COMSOL, Stockholm, Sweden).
781 (Fig. 4A). The 3D simulation domain of the modeled canal was a liquid column with a
782 length of 200 μm and a half-ellipse cross-sectional profile (the major and minor axis
783 being 150 μm and 10 μm, respectively). We assumed a free-slip boundary condition at
784 the upper interface of the domain (liquid-air interface) and non-slip boundary condition at
785 the lower boundary (liquid-solid interface). A surface tension gradient was loaded at the
786 liquid-air interface, while the pressure at both ends of the simulation domain was set as
787 zero. The fluid viscosity was set as 0.012 $\mathrm{Pa \cdot s}$, accordingly to a rheological
788 measurement of *P. aeruginosa* colony extracts (Fauvart et al., 2012). The simulation
789 was performed with a fine finite element mesh. Final results of stationary solution of
790 Navier-Stokes equation in the simulation domain were imported into MATLAB for data
791 processing. The surface and the bulk flow speed profiles were obtained by averaging
792 the flow speed in regions >50 μm away from both ends.

793

794 **Isolation, staining, and imaging of outer membrane vesicles (OMVs)**

795

796 To examine whether directed fluid flows in canals can facilitate long-range transport of
797 OMVs produced by *P. aeruginosa*, we isolated OMVs from bacterial culture by
798 centrifugation, labeled them fluorescently, and loaded the OMV dispersion into canals by
799 microinjection. We isolated and stained *P. aeruginosa* OMVs using the following
800 procedures. 200 mL of PA14 *flgK*::Tn5 overnight culture grown in M9DCAA medium
801 was centrifuged at 5000 x g for 5 min in 50 mL centrifuge tubes. The pellet and the
802 supernatant (containing OMVs) were collected and stored separately. The supernatant
803 was forced to pass through a 0.45 μm syringe filter, yielding a raw OMV dispersion with
804 all particulate matter greater than 0.45 μm in size removed. The raw OMV dispersion
805 was further purified and concentrated by centrifugation at 3000 x g for 5 min in
806 centrifugal devices with a cut-off molecular weight of 100 kDa (Microsep, Pall
807 Corporation), yielding ~500 μL final OMV dispersion in phosphate-buffered saline (PBS;
808 pH=7.0). The obtained OMV dispersion was then transferred to a glass test tube for

fluorescent staining with the membrane dye FM 1-43FX (Cat. No. F35355; Thermo Fisher Scientific). 5 µL of FM 1-43FX stock solution (1 mg/mL in DMSO) was added to the test tube and staining was allowed to proceed for 1 hr in a shaker (30 ºC and 180 rpm). To remove unreacted dyes, the volume of OMV dispersion in test tube was adjusted to 5.5 mL with PBS, and ~1/3 of the stored bacterial pellet was added to the test tube in order to absorb the unreacted dyes; the test tube was replaced in the shaker (30 ºC and 180 rpm) and incubated for 5 min, followed by centrifugation at 3000 x g for 5 min. The supernatant (containing fluorescently labeled OMVs) was again adjusted to a volume of ~5.5 mL with PBS and the procedures described above were repeated until using up the stored cell pellet. The resulting supernatant was forced to pass through a 0.45 µm syringe filter to remove cells, and then was purified and concentrated by centrifugation with the 100 kDa centrifugal devices as described above, yielding ~200 µL fluorescently labeled OMV dispersion in PBS. The size distribution of OMVs isolated this way was characterized by a particle sizer (NanoSight LM10, Malvern Instruments). The OMVs had a size ranging from ~30 nm to ~600 nm, with a mean size of ~150 nm (Fig. S5).

Microinjection of OMVs into canals was performed using an XYZ micromanipulator (M-562-XYZ, Newport Corporation) and a 100 µL microsyringe with a glass micropipette (20 µm in diameter, fabricated by hand-pulling a 0.5 mm glass capillary tube) attached to it. The setup was installed by the side of the stage of an inverted microscope (Nikon Ti-E), where the petri dish was placed. Prior to microinjection, fluorescently labeled OMV dispersion as described above was loaded into the microsyringe, and the lid of the petri dish was removed. Under the microscope via a 4X dark phase objective (N.A. 0.13), the glass micropipette was positioned to be just above the center of a canal at ~15 mm from the canal tip, and approximately 200 nL of OMV dispersion was dispensed to the canal by pushing the microsyringe. Immediately following the microinjection, the lid of petri dished was replaced, and the transport of OMVs in the canal was imaged using a 10X objective (N.A. 0.25) and a TRITC filter set (excitation: 535/50 nm, emission: 610/75 nm, dichroic: 565 nm long pass filter; Semrock) with the excitation light provided by a mercury precentered fiber illuminator (Intensilight, Nikon). Recordings were made with an sCMOS camera (Andor Zyla 4.2) with an exposure time of 0.1 s (for taking real time videos as shown in Movie S10) or 1 s (for acquiring OMV trajectories as shown in Fig. 5C). The final distribution of dispensed OMVs along the canal as shown in Fig. 5A,B

was imaged via a 4X objective (N.A. 0.13) with an exposure time of 1 s and the images at different locations were stitched by the software NIS Elements AR.

Interaction between *S. aureus* and *P. aeruginosa* colonies

We used *S. aureus* cells harboring a plasmid with constitutive GFP expression (Toledo-Arana et al., 2005), so that the cell mass in *S. aureus* colonies can be quantified by GFP fluorescence during the interaction with *P. aeruginosa*. Overnight cultures of *S. aureus* and *P. aeruginosa* PA14 were inoculated at different sides of an M9DCAAP agar plate. After incubating at 30 ºC for ~20 hr, the *P. aeruginosa* colony branches were approaching *S. aureus* colonies, and then we moved the plate onto the stage of an inverted microscope (Nikon Ti-E) for imaging. Phase contrast images were acquired with a 4X phase contrast objective (N.A. 0.13). Fluorescence images were acquired with a 10X objective (N.A. 0.25) and a FITC filter set (excitation: 482/35 nm, emission: 536/40 nm, dichroic: 506 nm long pass filter; Semrock), with the excitation light provided by an LED light source (X-Cite XLED1, Excelitas Technologies Corp.). To compute fluorescence count in the images, the background (acquired at a region with no cells) was first subtracted from the fluorescent images. To correct for the inhomogeneity of excitation illumination, the illumination intensity field was acquired by taking fluorescence images of a ~100 μm thick 0.55% agar pad infused with 10 μg/ml calcein (C0875, Sigma-Aldrich) that was placed on agar surface under the same imaging setup, and then the background-subtracted fluorescence images was divided by the illumination intensity field. The agar pad was made by solidifying molten agar between two cover glasses. *S. aureus* colony biomass was measured by the total background-corrected fluorescence count in the area originally occupied by the colony prior to contact with *P. aeruginosa*.

868 **References**

869

870 Andersen, J. B., Sternberg, C., Poulsen, L. K., Bjørn, S. P., Givskov, M., & Molin, S.
871 (1998). New Unstable Variants of Green Fluorescent Protein for Studies of Transient
872 Gene Expression in Bacteria. *Applied and Environmental Microbiology, 64*(6), 2240-
873 2246. doi: doi:10.1128/AEM.64.6.2240-2246.1998
874 Angelini, T. E., Roper, M., Kolter, R., Weitz, D. A., & Brenner, M. P. (2009). Bacillus
875 subtilis spreads by surfing on waves of surfactant. *Proceedings of the National
876 Academy of Sciences, 106*(43), 18109-18113. doi: 10.1073/pnas.0905890106
877 Beaussart, A., Baker, A. E., Kuchma, S. L., El-Kirat-Chatel, S., O'Toole, G. A., & Dufrêne,
878 Y. F. (2014). Nanoscale adhesion forces of Pseudomonas aeruginosa type IV Pili.
879 *ACS nano, 8*(10), 10723-10733. doi: 10.1021/nn5044383
880 Berg, H. C. (1993). *Random Walks in Biology*: Princeton, Princeton, NJ.
881 Bomberger, J. M., Maceachran, D. P., Coutermarsh, B. A., Ye, S., O'Toole, G. A., &
882 Stanton, B. A. (2009). Long-distance delivery of bacterial virulence factors by
883 Pseudomonas aeruginosa outer membrane vesicles. *PLoS Pathog, 5*(4), e1000382.
884 doi: 10.1371/journal.ppat.1000382
885 Brenner, K., You, L., & Arnold, F. H. (2008). Engineering microbial consortia: a new
886 frontier in synthetic biology. *Trends in Biotechnology, 26*(9), 483-489. doi:
887 https://doi.org/10.1016/j.tibtech.2008.05.004
888 Cao, Y., Ryser, Marc D., Payne, S., Li, B., Rao, Christopher V., & You, L. (2016).
889 Collective Space-Sensing Coordinates Pattern Scaling in Engineered Bacteria. *Cell,
890 165*(3), 620-630. doi: 10.1016/j.cell.2016.03.006
891 Chandler, D. (1987). *Introduction to Modern Statistical Mechanics*: Oxford University
892 Press.
893 Chen, Y., Kim, J. K., Hirning, A. J., Josić, K., & Bennett, M. R. (2015). Emergent genetic
894 oscillations in a synthetic microbial consortium. *Science, 349*(6251), 986-989. doi:
895 10.1126/science.aaa3794
896 Chew, S. C., Yam, J. K. H., Matysik, A., Seng, Z. J., Klebensberger, J., Givskov, M., . . .
897 Kjelleberg, S. (2018). Matrix Polysaccharides and SiaD Diguanylate Cyclase Alter
898 Community Structure and Competitiveness of Pseudomonas aeruginosa
899 during Dual-Species Biofilm Development with Staphylococcus aureus.
900 *mBio, 9*(6), e00585-00518. doi: 10.1128/mBio.00585-18
901 Davey, M. E., Caiazza, N. C., & O'Toole, G. A. (2003). Rhamnolipid surfactant production

902 affects biofilm architecture in Pseudomonas aeruginosa PAO1. *J Bacteriol, 185*(3),
903 1027-1036. doi: 10.1128/jb.185.3.1027-1036.2003
904 de Gennes, P. G., Brochard-Wyart, F., & Quere, D. (2003). *Capillarity and Wetting*
905 *Phenomena: Drops, Bubbles, Pearls, Waves*: Springer New York.
906 Divoux, T., Fardin, M. A., Manneville, S., & Lerouge, S. (2016). Shear Banding of
907 Complex Fluids. *Annual Review of Fluid Mechanics, 48*(1), 81-103. doi:
908 10.1146/annurev-fluid-122414-034416
909 Drury, W. J., Characklis, W. G., & Stewart, P. S. (1993). Interactions of 1 μm latex
910 particles with Pseudomonas aeruginosa biofilms. *Water Research, 27*(7), 1119-1126.
911 Du, H., Xu, Z., Anyan, M., Kim, O., Leevy, W. M., Shrout, Joshua D., & Alber, M. (2012).
912 High Density Waves of the Bacterium Pseudomonas aeruginosa in Propagating
913 Swarms Result in Efficient Colonization of Surfaces. *Biophysical Journal, 103*(3), 601-
914 609. doi: http://dx.doi.org/10.1016/j.bpj.2012.06.035
915 Faubel, R., Westendorf, C., Bodenschatz, E., & Eichele, G. (2016). Cilia-based flow
916 network in the brain ventricles. *Science, 353*(6295), 176-178. doi:
917 10.1126/science.aae0450
918 Fauvart, M., Phillips, P., Bachaspatimayum, D., Verstraeten, N., Fransaer, J., Michiels,
919 J., & Vermant, J. (2012). Surface tension gradient control of bacterial swarming in
920 colonies of Pseudomonas aeruginosa. *Soft Matter, 8*(1), 70-76. doi:
921 10.1039/c1sm06002c
922 Fenchel, T., & Glud, R. N. (1998). Veil architecture in a sulphide-oxidizing bacterium
923 enhances countercurrent flux. *Nature, 394*(6691), 367-369. doi: 10.1038/28609
924 Gdaniec, B. G., Bonini, F., Prodon, F., Braschler, T., Köhler, T., & van Delden, C. (2022).
925 Pseudomonas aeruginosa rhamnolipid micelles deliver toxic metabolites and
926 antibiotics into Staphylococcus aureus. *iScience, 25*(1), 103669. doi:
927 https://doi.org/10.1016/j.isci.2021.103669
928 Guo, S., Samanta, D., Peng, Y., Xu, X., & Cheng, X. (2018). Symmetric shear banding
929 and swarming vortices in bacterial superfluids. *Proceedings of the National Academy*
930 *of Sciences, 115*(28), 7212-7217. doi: 10.1073/pnas.1722505115
931 Hanyak, M., Sinz, D. K. N., & Darhuber, A. A. (2012). Soluble surfactant spreading on
932 spatially confined thin liquid films. *Soft Matter, 8*(29), 7660-7671. doi:
933 10.1039/C2SM25484K
934 Hentzer, M., Riedel, K., Rasmussen, T. B., Heydorn, A., Andersen, J. B., Parsek, M.
935 R., . . . Givskov, M. (2002). Inhibition of quorum sensing in Pseudomonas aeruginosa

biofilm bacteria by a halogenated furanone compound. *Microbiology (Reading), 148*(Pt 1), 87-102. doi: 10.1099/00221287-148-1-87

Hotterbeekx, A., Kumar-Singh, S., Goossens, H., & Malhotra-Kumar, S. (2017). In vivo and In vitro Interactions between Pseudomonas aeruginosa and Staphylococcus spp. *Frontiers in Cellular and Infection Microbiology, 7*(106). doi: 10.3389/fcimb.2017.00106

Huang, B. K., & Choma, M. A. (2015). Microscale imaging of cilia-driven fluid flow. *Cellular and molecular life sciences : CMLS, 72*(6), 1095-1113. doi: 10.1007/s00018-014-1784-z

Kearns, D. B. (2010). A field guide to bacterial swarming motility. *Nat. Rev. Microbiol., 8*, 634-644.

Kong, W., Meldgin, D. R., Collins, J. J., & Lu, T. (2018). Designing microbial consortia with defined social interactions. *Nature Chemical Biology, 14*(8), 821-829. doi: 10.1038/s41589-018-0091-7

Lang, S., & Wullbrandt, D. (1999). Rhamnose lipids--biosynthesis, microbial production and application potential. *Appl Microbiol Biotechnol, 51*(1), 22-32. doi: 10.1007/s002530051358

Lavrentovich, M. O., Koschwanez, J. H., & Nelson, D. R. (2013). Nutrient shielding in clusters of cells. *Physical Review E, 87*(6), 062703.

Lee, D. D., Prindle, A., Liu, J., & Süel, G. M. (2017). SnapShot: Electrochemical Communication in Biofilms. *Cell, 170*(1), 214-214.e211. doi: 10.1016/j.cell.2017.06.026

Lee, K., Hahn, L. D., Yuen, W. W., Vlamakis, H., Kolter, R., & Mooney, D. J. (2011). Metal-Enhanced Fluorescence to Quantify Bacterial Adhesion. *Advanced Materials, 23*(12), H101-H104. doi: https://doi.org/10.1002/adma.201004096

Liu, S., Shankar, S., Marchetti, M. C., & Wu, Y. (2021). Viscoelastic control of spatiotemporal order in bacterial active matter. *Nature, 590*(7844), 80-84. doi: 10.1038/s41586-020-03168-6

Luo, N., Wang, S., Lu, J., Ouyang, X., & You, L. (2021). Collective colony growth is optimized by branching pattern formation in Pseudomonas aeruginosa. *Molecular Systems Biology, 17*(4), e10089. doi: https://doi.org/10.15252/msb.202010089

Luzar, M. A., Thomassen, M. J., & Montie, T. C. (1985). Flagella and motility alterations in Pseudomonas aeruginosa strains from patients with cystic fibrosis: relationship to patient clinical condition. *Infect Immun, 50*(2), 577-582. doi: 10.1128/iai.50.2.577-

582.1985

Mahenthiralingam, E., Campbell, M. E., & Speert, D. P. (1994). Nonmotility and phagocytic resistance of Pseudomonas aeruginosa isolates from chronically colonized patients with cystic fibrosis. *Infect Immun, 62*(2), 596-605. doi: 10.1128/iai.62.2.596-605.1994

Martinez, V. A., Clément, E., Arlt, J., Douarche, C., Dawson, A., Schwarz-Linek, J., . . . Poon, W. C. K. (2020). A combined rheometry and imaging study of viscosity reduction in bacterial suspensions. *Proceedings of the National Academy of Sciences, 117*(5), 2326-2331. doi: 10.1073/pnas.1912690117

Mashburn, L. M., & Whiteley, M. (2005). Membrane vesicles traffic signals and facilitate group activities in a prokaryote. *Nature, 437*, 422-425.

Miano, A., Liao, M. J., & Hasty, J. (2020). Inducible cell-to-cell signaling for tunable dynamics in microbial communities. *Nature Communications, 11*(1), 1193. doi: 10.1038/s41467-020-15056-8

Mitchell, J. G., & Kogure, K. (2006). Bacterial motility: links to the environment and a driving force for microbial physics. *FEMS Microbiology Ecology, 55*(1), 3-16. doi: 10.1111/j.1574-6941.2005.00003.x

Mukherjee, S., & Bassler, B. L. (2019). Bacterial quorum sensing in complex and dynamically changing environments. *Nature Reviews Microbiology, 17*(6), 371-382. doi: 10.1038/s41579-019-0186-5

Müller, M. M., Kügler, J. H., Henkel, M., Gerlitzki, M., Hörmann, B., Pöhnlein, M., . . . Hausmann, R. (2012). Rhamnolipids—Next generation surfactants? *Journal of Biotechnology, 162*(4), 366-380. doi: https://doi.org/10.1016/j.jbiotec.2012.05.022

Nelson, P. (2003). *Biological Physics (Updated Edition)*: W. H. Freeman.

O'Toole, G. A., & Wong, G. C. (2016). Sensational biofilms: surface sensing in bacteria. *Curr Opin Microbiol, 30*, 139-146. doi: 10.1016/j.mib.2016.02.004

Ochsner, U. A., Fiechter, A., & Reiser, J. (1994). Isolation, characterization, and expression in Escherichia coli of the Pseudomonas aeruginosa rhlAB genes encoding a rhamnosyltransferase involved in rhamnolipid biosurfactant synthesis. *Journal of Biological Chemistry, 269*(31), 19787-19795.

Olmsted, P. D. (2008). Perspectives on shear banding in complex fluids. *Rheologica Acta, 47*(3), 283-300. doi: 10.1007/s00397-008-0260-9

Ovarlez, G., Rodts, S., Chateau, X., & Coussot, P. (2009). Phenomenology and physical origin of shear localization and shear banding in complex fluids. *Rheologica Acta,*

48(8), 831-844. doi: 10.1007/s00397-008-0344-6

Parsek, M. R., & Greenberg, E. P. (2005). Sociomicrobiology: the connections between quorum sensing and biofilms. *Trends Microbiol, 13*(1), 27-33.

Payne, S., Li, B., Cao, Y., Schaeffer, D., Ryser, M. D., & You, L. (2013). Temporal control of self-organized pattern formation without morphogen gradients in bacteria. *Mol Syst Biol, 9*, 697. doi: 10.1038/msb.2013.55

Persat, A., Nadell, C. D., Kim, M. K., Ingremeau, F., Siryaporn, A., Drescher, K., . . . Stone, H. A. (2015). The mechanical world of bacteria. *Cell, 161*(5), 988-997. doi: 10.1016/j.cell.2015.05.005

Petroff, A., & Libchaber, A. (2014). Hydrodynamics and collective behavior of the tethered bacterium Thiovulum majus. *Proceedings of the National Academy of Sciences, 111*(5), E537-E545. doi: 10.1073/pnas.1322092111

PIRT, S. J. (1967). A Kinetic Study of the Mode of Growth of Surface Colonies of Bacteria and Fungi. *Microbiology, 47*(2), 181-197. doi: doi:10.1099/00221287-47-2-181

Ramos, I., Dietrich, L. E. P., Price-Whelan, A., & Newman, D. K. (2010). Phenazines affect biofilm formation by Pseudomonas aeruginosa in similar ways at various scales. *Research in Microbiology, 161*(3), 187-191. doi: 10.1016/j.resmic.2010.01.003

Rhodeland, B., Hoeger, K., & Ursell, T. (2020). Bacterial surface motility is modulated by colony-scale flow and granular jamming. *Journal of The Royal Society Interface, 17*(167), 20200147. doi: doi:10.1098/rsif.2020.0147

Roché, M., Li, Z., Griffiths, I. M., Le Roux, S., Cantat, I., Saint-Jalmes, A., & Stone, H. A. (2014). Marangoni Flow of Soluble Amphiphiles. *Physical Review Letters, 112*(20), 208302. doi: 10.1103/PhysRevLett.112.208302

Ron, E. Z., & Rosenberg, E. (2001). Natural roles of biosurfactants. *Environ Microbiol, 3*(4), 229-236.

Rooney, L. M., Amos, W. B., Hoskisson, P. A., & McConnell, G. (2020). Intra-colony channels in E. coli function as a nutrient uptake system. *The ISME journal, 14*(10), 2461-2473. doi: 10.1038/s41396-020-0700-9

Sack, L., & Holbrook, N. M. (2006). LEAF HYDRAULICS. *Annual Review of Plant Biology, 57*(1), 361-381. doi: 10.1146/annurev.arplant.56.032604.144141

Scallan, J. P., Zawieja, S. D., Castorena-Gonzalez, J. A., & Davis, M. J. (2016). Lymphatic pumping: mechanics, mechanisms and malfunction. *The Journal of physiology, 594*(20), 5749-5768. doi: 10.1113/JP272088

1038 Schulz, H. N., & Jorgensen, B. B. (2001). Big bacteria. *Annu Rev Microbiol, 55*, 105-137.
1039 doi: 10.1146/annurev.micro.55.1.105
1040 Schwechheimer, C., & Kuehn, M. J. (2015). Outer-membrane vesicles from Gram-
1041 negative bacteria: biogenesis and functions. *Nature Reviews Microbiology, 13*(10),
1042 605-619. doi: 10.1038/nrmicro3525
1043 Shao, X., Mugler, A., Kim, J., Jeong, H. J., Levin, B. R., & Nemenman, I. (2017). Growth
1044 of bacteria in 3-d colonies. *PLOS Computational Biology, 13*(7), e1005679. doi:
1045 10.1371/journal.pcbi.1005679
1046 Shapiro, J. A. (1998). Thinking about bacterial populations as multicellular organisms.
1047 *Annu. Rev. Microbiol., 52*, 81-104.
1048 Soares Dos Santos, A., Pereira, N., Jr., & Freire, D. M. (2016). Strategies for improved
1049 rhamnolipid production by Pseudomonas aeruginosa PA1. *PeerJ, 4*, e2078. doi:
1050 10.7717/peerj.2078
1051 Stoodley, P., DeBeer, D., & Lewandowski, Z. (1994). Liquid flow in biofilm systems.
1052 *Applied and Environmental Microbiology, 60*(8), 2711-2716.
1053 Talà, L., Fineberg, A., Kukura, P., & Persat, A. (2019). Pseudomonas aeruginosa
1054 orchestrates twitching motility by sequential control of type IV pili movements. *Nature*
1055 *Microbiology, 4*(5), 774-780. doi: 10.1038/s41564-019-0378-9
1056 Toledo-Arana, A., Merino, N., Vergara-Irigaray, M., Débarbouillé, M., Penadés, J. R., &
1057 Lasa, I. (2005). Staphylococcus aureus develops an alternative, ica-independent
1058 biofilm in the absence of the arlRS two-component system. *Journal of Bacteriology,*
1059 *187*(15), 5318-5329. doi: 10.1128/JB.187.15.5318-5329.2005
1060 Tremblay, J., & Déziel, E. (2010). Gene expression in Pseudomonas aeruginosa
1061 swarming motility. *BMC Genomics, 11*, 587.
1062 Trinschek, S., John, K., & Thiele, U. (2018). Modelling of surfactant-driven front
1063 instabilities in spreading bacterial colonies. *Soft Matter, 14*(22), 4464-4476. doi:
1064 10.1039/C8SM00422F
1065 Troian, S. M., Wu, X. L., & Safran, S. A. (1989). Fingering instability in thin wetting films.
1066 *Phys Rev Lett, 62*(13), 1496-1499.
1067 van Gestel, J., Vlamakis, H., & Kolter, R. (2015). Division of Labor in Biofilms: the
1068 Ecology of Cell Differentiation. *Microbiol Spectr, 3*(2), Mb-0002-2014. doi:
1069 10.1128/microbiolspec.MB-0002-2014
1070 Whitesides, G. M., Ostuni, E., Takayama, S., Jiang, X., & Ingber, D. E. (2001). Soft
1071 lithography in biology and biochemistry. *Annu Rev Biomed Eng, 3*, 335-373.

1072 Wilking, J. N., Zaburdaev, V., De Volder, M., Losick, R., Brenner, M. P., & Weitz, D. A.
1073 (2013). Liquid transport facilitated by channels in Bacillus subtilis biofilms.
1074 *Proceedings of the National Academy of Sciences, 110*(3), 848-852. doi:
1075 10.1073/pnas.1216376110
1076 Wolfgang, M. C., Jyot, J., Goodman, A. L., Ramphal, R., & Lory, S. (2004).
1077 Pseudomonas aeruginosa regulates flagellin expression as part of a global response
1078 to airway fluid from cystic fibrosis patients. *Proc Natl Acad Sci U S A, 101*(17), 6664-
1079 6668. doi: 10.1073/pnas.0307553101
1080 Wu, X.-L., & Libchaber, A. (2000). Particle diffusion in a quasi-two-dimensional bacterial
1081 bath. *Phys. Rev. Lett., 84*, 3017-3020.
1082 Wu, Y., & Berg, H. C. (2012). Water reservoir maintained by cell growth fuels the
1083 spreading of a bacterial swarm. *Proc Natl Acad Sci U S A, 109*(11), 4128-4133.
1084 Wu, Y., Hosu, B. G., & Berg, H. C. (2011). Microbubbles reveal chiral fluid flows in
1085 bacterial swarms. *Proc Natl Acad Sci U S A, 108*(10), 4147-4151.
1086 Xu, H., Dauparas, J., Das, D., Lauga, E., & Wu, Y. (2019). Self-organization of swimmers
1087 drives long-range fluid transport in bacterial colonies. *Nature Communications, 10*(1),
1088 1792. doi: 10.1038/s41467-019-09818-2
1089 Yang, L., Rybtke, M. T., Jakobsen, T. H., Hentzer, M., Bjarnsholt, T., Givskov, M., &
1090 Tolker-Nielsen, T. (2009). Computer-Aided Identification of Recognized Drugs as
1091 Pseudomonas aeruginosa Quorum-Sensing Inhibitors. *Antimicrobial*
1092 *Agents and Chemotherapy, 53*(6), 2432-2443. doi: 10.1128/aac.01283-08
1093 Zhao, F., Shi, R., Ma, F., Han, S., & Zhang, Y. (2018). Oxygen effects on rhamnolipids
1094 production by Pseudomonas aeruginosa. *Microbial Cell Factories, 17*(1), 39. doi:
1095 10.1186/s12934-018-0888-9
1096 Zuo, W., & Wu, Y. (2020). Dynamic motility selection drives population segregation in a
1097 bacterial swarm. *Proceedings of the National Academy of Sciences, 117*(9), 4693-
1098 4700. doi: 10.1073/pnas.1917789117

Acknowledgement. We thank Roberto Kolter (Harvard University) and George A. O'Toole (Dartmouth College) for providing the bacterial strains; Peter Greenberg (University of Washington) for helpful comments and for providing bacterial strains; To Ngai and Hang Jiang (CUHK) for assistance with surface tension measurement; Shannon Au (CUHK) for help with membrane vesicle isolation; and Bo Zheng and Qi Liu (CUHK) for help with PDMS microfluidic chip fabrication. We also thank Qihui Hou for helpful discussion and information on rhamnolipid control of colony patterns. This work was supported by the National Natural Science Foundation of China (NSFC No. 31971182, to Y.W.), the Research Grants Council of Hong Kong SAR (RGC Ref. No. 14303918, RFS2021-4S04 and CUHK Direct Grants; to Y.W.), Guangdong Natural Science Foundation for Distinguished Young Scholar (No. 2020B1515020003, to L.Y.), and Guangdong Basic and Applied Basic Research Foundation (No. 2019A1515110640, to Y.Z.).

Author Contributions: Y.L. designed the study, performed experiments, analyzed and interpreted the data. S.L. performed experiments, analyzed and interpreted the data. Y.Z. helped with manuscript preparation. Z.J.S. constructed the *rhlA* mutant. H.X. performed experiments. L.Y. provided materials and designed the study. Y.W. conceived and designed the study, analyzed and interpreted the data. L.Y. and Y.W. supervised the study. Y.W. wrote the paper with input from other authors.

Competing interests: The authors declare no competing financial interests.

Data and materials availability: All data are available in the main text or the Supplementary Information.

Figures

Figure 1

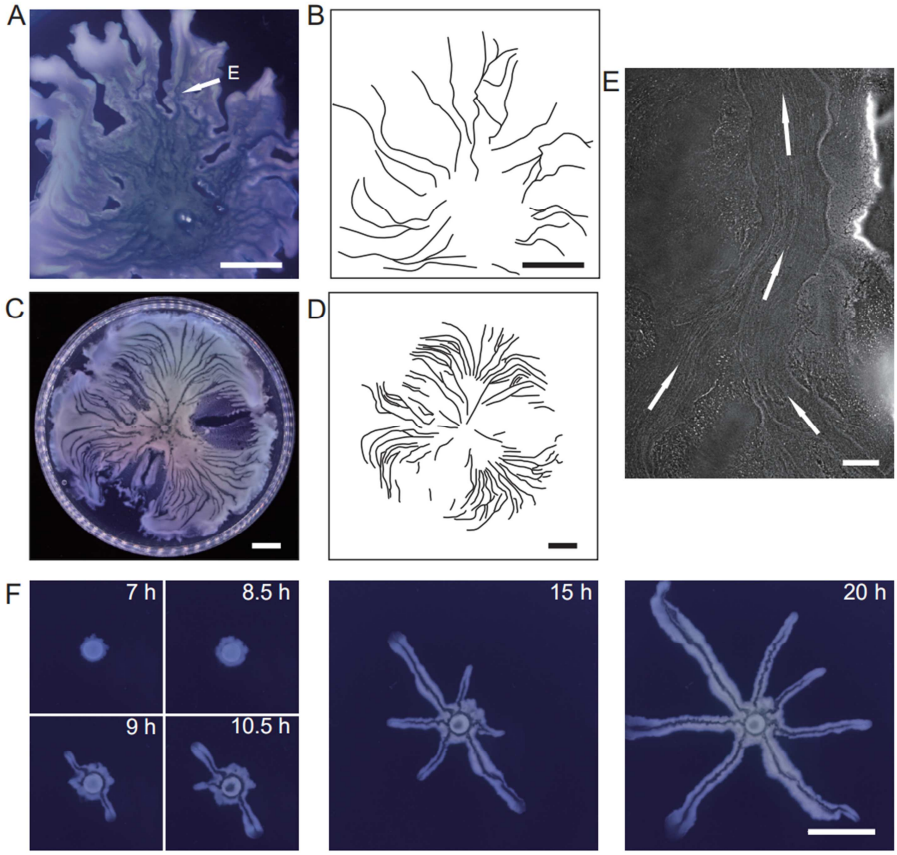

Fig. 1. Large-scale open channels in non-flagellated *P. aeruginosa* colonies support directed fluid transport. (A) Colony morphology of non-motile *P. aeruginosa* (PA14 *flgK*::Tn5 Δ*pilA*). The arrow indicates the position where the image in panel E was taken. (B) Sketch of the open channels in panel A for better visualization. (C) Colony morphology of piliated *P. aeruginosa* (PA14 *flgK*::Tn5). (D) Sketch of the open channels in panel C for better visualization. Scale bars in A-D, 1 cm. (E) Phase contrast microscopy image of an open channel with cellular flows in a non-motile *P. aeruginosa* (PA14 *flgK*::Tn5 Δ*pilA*) colony, taken at the location indicated by the arrow in panel A. Arrows indicate flow direction. Scale bar, 100 μm. Cellular flows in the open channel are better visualized in Movie S2 because the contrast between the open channel and other regions is low in still images. (F) Time-lapse image sequence showing the

development of open channels in branching colonies of piliated *P. aeruginosa* (PA14 *flgK*::Tn5). Scale bar, 1 cm. Also see Movie S5.

1148 Figure 2

1149

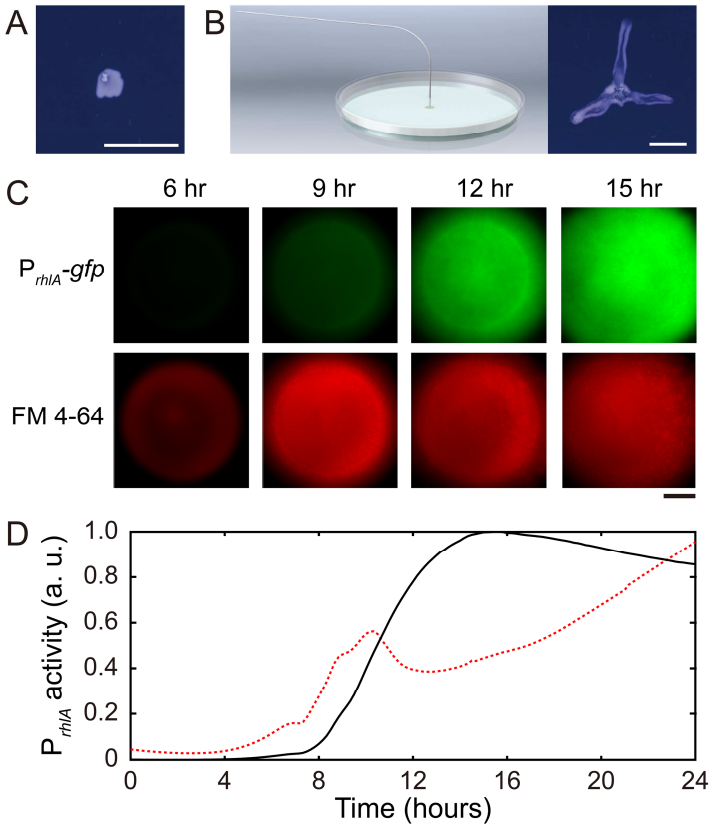

1150

1151 **Fig. 2**. **Role of rhamnolipids in canal development**. (A) Image of a representative
1152 colony of the rhamnolipid-deficient mutant (PA14 flgK::Tn5 Δ*rhlA*) after 20 hr growth.
1153 The colony failed to develop canals and microscopic flows. (B) Surface tension gradient
1154 established by 1-hr injection of exogenous rhamnolipids at the colony center following
1155 20-hr growth (schematics shown as left panel; Methods) restored the formation of canals
1156 (right panel). Scale bars in A,B, 1 cm. (C) Fluorescence image sequences showing
1157 promoter activity of rhamnolipid synthesis at the early stage of canal development. The
1158 images were taken at the center of representative canal-forming *P. aeruginosa* colonies
1159 (PA14 *flgK*::Tn5) grown at room temperature. The upper row shows GFP(ASV)
1160 fluorescence from the rhamnolipid synthesis reporter P_{rhlA}-*gfp(ASV)* (Methods), and the
1161 lower row shows red fluorescence of the membrane dye FM 4-64, which serves as a
1162 proxy of cell number in the colony. Scale bar, 1 mm. (D) Temporal dynamics of
1163 rhamnolipid synthesis level measured by the fluorescence of P_{rhlA}-*gfp(ASV)* reporter
1164 during canal development. Solid and dashed lines represent the overall fluorescence
1165 count of the rhamnolipid synthesis reporter and the FM 4-64 dye, respectively

(Methods). The colony started to expand at T=~10 hr, and the expansion caused a slight drop of overall FM 4-64 fluorescence count during T= ~10-12 hr. Three replicate experiments were performed and they showed the same temporal dynamics.

1169 Figure 3

1170

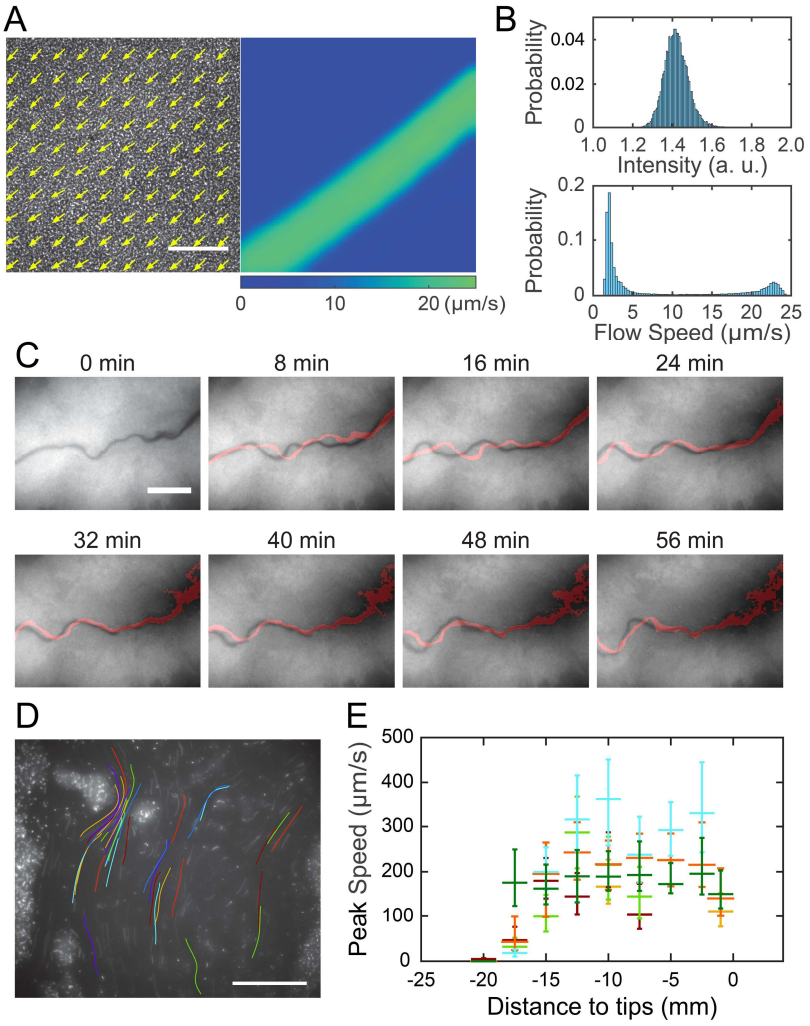

1171

1172

1173 **Fig. 3**. **Shear-induced banding during canal development and flow speed profile in**

1174 **canals**. (A) Collective velocity field of cells in a region with homogeneous cell density

1175 distribution prior to canal formation. The collective velocity field was measured by

1176 particle image velocimetry (PIV) analysis on phase-contrast image sequence and

1177 averaged over a time window of 4 s (Methods). Arrows in left panel and colormap in

1178 right panel represent collective velocity direction and magnitude, respectively. The

1179 velocity direction field in left panel is superimposed onto the phase-contrast image of this

1180 region. Both panels share the same scale bar (100 □m). Also see Movie S8. (B)

1181 Probability distributions of phase-contrast image intensity (upper panel) and flow speed

1182 (lower panel) associated with panel A. Unimodal distribution of phase-contrast intensity

indicates a homogeneous distribution of cell density. The bimodal distribution of flow speeds shows the occurrence of a high-speed flow regime. (C) Image sequence showing the course of a developing canal in a colony. Cells in the colony hosted the GFP-reporter plasmid expressing P_{rhlA}-*gfp*(*ASV*) and the colony was imaged by fluorescence microscopy (Methods). The course of the canal (across the center of each image) had lower cell density due to flushing by rapid flows and thus appeared darker than other areas. The red trace in each image starting from T= 8 min indicates the course of the canal in the previous image (8 min earlier). Scale bar, 125 μm. Also see Movie S9. (D) The fluorescence image of a canal in a *P. aeruginosa* colony seeded with ~1% GFP-expressing cells. The image was taken at a distance of ~12.5 mm from the tip of a canal. Colored traces show the trajectories of 38 fluorescent cells being transported in the canal, which were recorded during 0.5 s exposure time of a single image frame. Scale bar, 100 μm. Different colors serve to distinguish trajectories of different cells. (E) Peak flow speed at different locations of canals. The horizontal axis indicates the distance from the canal tips to the measuring position. Horizontal error bars indicate the uncertainty of canal position measurement (1 mm). Vertical error bars indicate the full range of peak speeds measured from >20 cell trajectories. Data from independent experiments are presented in different colors.

Figure 4

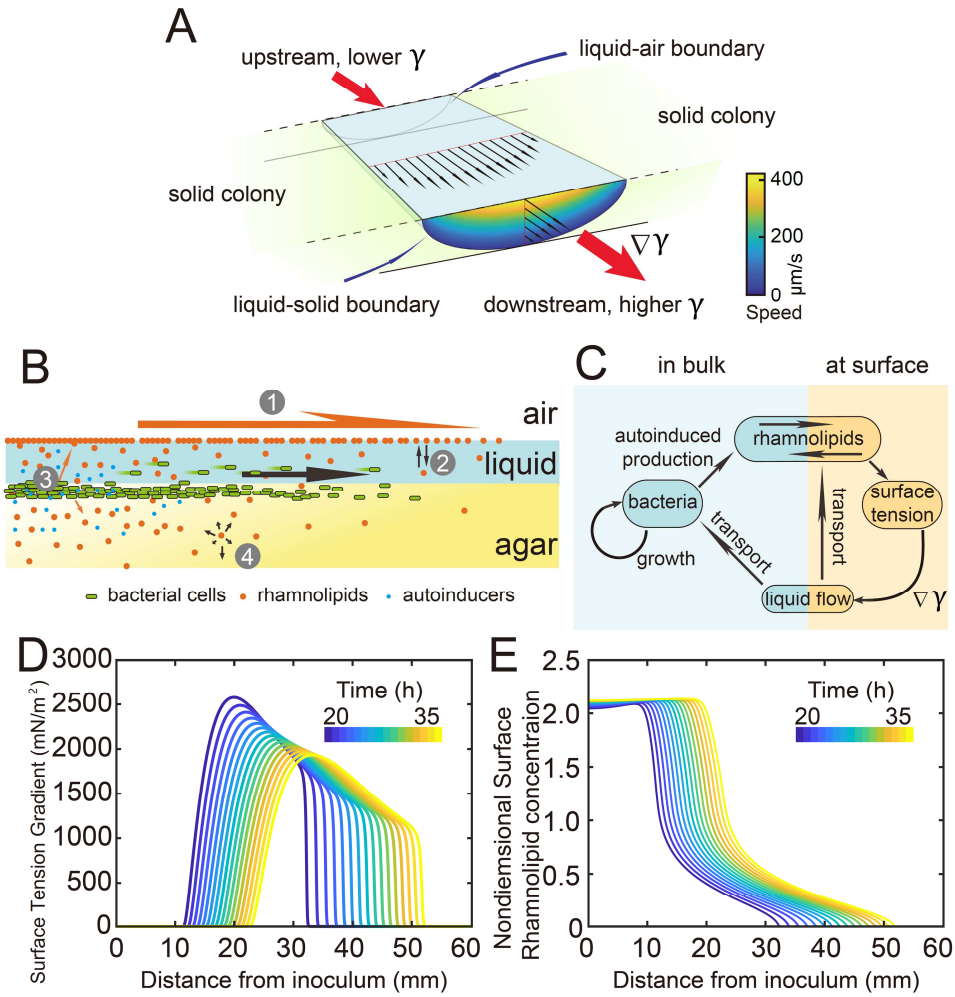

Fig. 4. **Modeling fluid transport and spatial-temporal dynamics of surface tension gradient in canals.** (A) Hydrodynamic simulation of fluid transport in a simplified canal geometry. The cross-sectional profile of the canal was modeled as a half ellipse with the major and minor axis being 150 μm and 10 μm, respectively. Note that the vertical and horizontal length scales are different. Red arrows indicate the direction of surface tension gradient $\nabla\gamma$. Black arrows and colormap show the surface and the bulk flow speed profiles, respectively, generated by a surface tension gradient of $1000\ \mathrm{mN}\cdot\mathrm{m}^{-2}$ imposed at the canal's upper surface (liquid-air boundary). (B) Schematic showing the key processes involved in the establishment of surface tension gradient in canals. Major constituents of the colony are represented by symbols of different colors: surfactant

molecules, orange dots; QS molecule, blue dots; cells, green rods. The key processes are labeled by numbers: “1”, transport of bacteria and biosurfactant at the liquid-air interface driven by surface tension gradient $\nabla\gamma$; “2”, biosurfactant exchange between the liquid-air interface and the bulk phase; “3”, growth of bacteria and the production of biosurfactant under QS regulation; “4”, diffusion of biosurfactant, QS molecules, and nutrient. Arrows indicate the direction of material transport. (C) Schematic showing the coupling of the key processes described in panel A and in main text. See SI Text for details. (D,E) Spatiotemporal dynamics of surface-associated surfactant concentration Γ and surface tension gradient $\nabla\gamma$ obtained by numerical simulations of the mathematical model, as shown in panels D and E, respectively. Also see Fig. S4 for the numerical result of the spatial-temporal evolution of other quantities in the model.

Figure 5

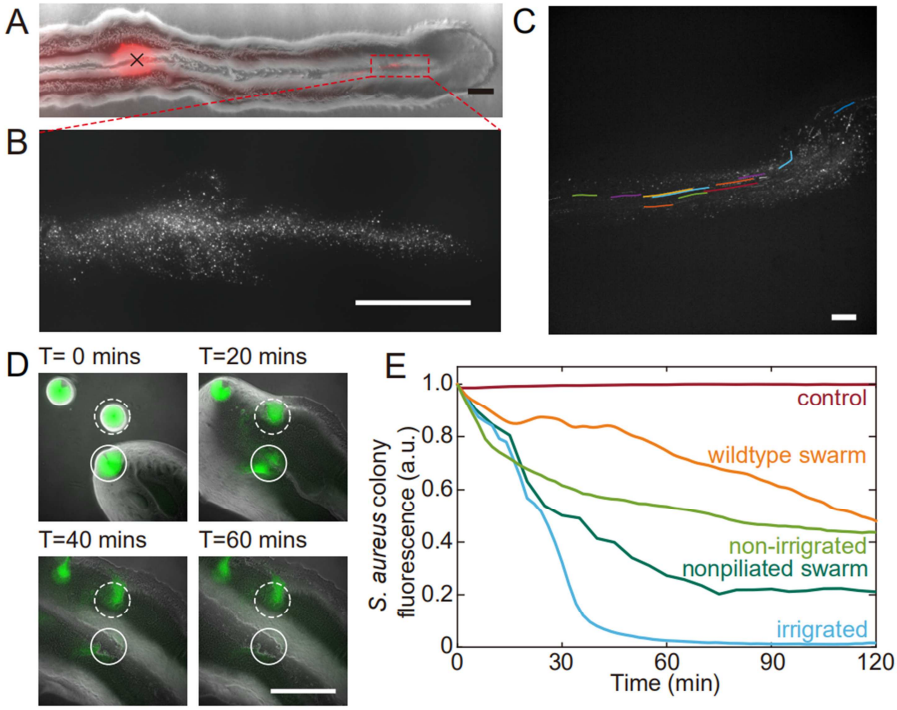

Fig. 5. Fluid flows in *P. aeruginosa* canals transport OMVs and help to eradicate *S. aureus* colonies. (A) Phase contrast image of a canal overlaid with the fluorescence image of OMVs (in red). The cross sign marks the location of microinjecting OMV dispersion. The loaded OMVs were transported downstream along the canal and accumulated near the tip. Scale bar, 1 mm. (B) Enlarged view of the OMV fluorescence image at the red dashed box in panel A. Scale bar, 500 μm. (C) Colored traces show the trajectories of fluorescently labeled OMVs during 1-s exposure time. Scale bar, 100 μm. Also see Movie S10. (D) Image sequence showing the eradication of an *S. aureus* colony (GFP-labelled, enclosed by the solid line) that was irrigated by *P. aeruginosa* canal flows. A nearby *S. aureus* colony (enclosed by the dashed line) came into contact with the *P. aeruginosa* colony but did not encounter canal flows. In each panel the fluorescence image of *S. aureus* colonies is superimposed onto the phase contrast image. Also see Movie S11. (E) Temporal dynamics of *S. aureus* colony biomass after encountering *P. aeruginosa* PA14 colonies under different conditions. To compare with the effect of potential material transport by flagellar motility (Y. Wu et al., 2011; Xu et al., 2019), curves labeled as “wildtype swarm” and “nonpiliated swarm” were shown for *S. aureus* colonies encountering wildtype *P. aeruginosa* (with both flagellar and type-IV

pilus motilities) and nonpiliated *P. aeruginosa* (PA14 Δ*pilB*; with flagellar motility alone), respecively (see Fig. S6 for details; Methods). At least three replicates were performed for each condition.

Supplementary Information for

Self-organized canals enable long range directed material transport in bacterial communities

Ye Li, Shiqi Liu, Yingdan Zhang, Zi Jing Seng, Haoran Xu, Liang Yang*, Yilin Wu *

*Corresponding authors. Email: ylwu@cuhk.edu.hk or yangl@sustech.edu.cn

This file includes:

Supplementary Text
Figs. S1 to S19
Tables S1 to S2
Legends for Movies S1 to S11

Other Supplementary Information for this manuscript include the following:

Movies S1 to S11

Supplementary Text (SI Text)

Mathematical model for the dynamics of surfactant distribution

A key component of our model for the spatial-temporal dynamics of surfactant distribution is biosurfactant exchange between the liquid-air interface and the bulk phase. The kinetics of biosurfactant exchange between the two phases could be learned from a relation between the bulk concentration and the surface concentration of biosurfactant at steady state.

Based on our measurement of surface tension at different rhamnolipid concentrations (Fig. S3), the relation between the steady-state surface tension γ_{ss} and bulk concentration of biosurfactant *c* can be well described by an exponential decay:

$$\gamma_{ss}(c) = \Pi_{\max} \exp(-c / c_s) + \gamma_\infty \quad \text{[S1]}$$

In Eq. [S1] $\Pi_{\max} = 41.6\ \mathrm{mN \cdot m^{-1}}$ is the maximal decrease of surface tension; $c_s = 12.9\ \mathrm{mg \cdot L^{-1}}$ is the characteristic concentration of rhamnolipids; $\gamma_\infty = 30.6\ \mathrm{mN \cdot m^{-1}}$ is the saturated surface tension of rhamnolipid solutions.

On the other hand, the surface tension directly depends on the surface concentration of surfactants (Γ). Such a relation is well fitted by a quadratic exponential decay (Hanyak et al., 2012):

$$\gamma(\Gamma) = \Pi_{max} exp(-A\Gamma^2 / \Gamma_c^{\ 2}) + \gamma_\infty \quad \text{[S2]}$$

In Eq. [S2], Γ_c is the characteristic surface concentration of surfactant, *A* is a parameter relating bulk surfactant concentration to the steady-state surface density of the surfactant.

Comparing Eq. [S2] to Eq. [S1], we find that $c \sim A\Gamma^2$ at equilibrium. This means that the surface concentration of rhamnilipids does not saturate but varies with the bulk concentration. To account for this behavior of rhamnilipids, we model the rate of biosurfactant transfer (r_{net}) from the bulk phase to the interface as follows:

$$r_{net} \propto \frac{c}{c_s} - A\frac{\Gamma^2}{\Gamma_c^2} = k(\frac{c}{c_s} - A\frac{\Gamma^2}{\Gamma_c^2}) \quad \text{[S3]}$$

In Eq. [S3], k is a reaction rate constant. To simplify the analysis, we introduced the dimensionless bulk concentration $c_n = c/c_s$ and the dimensionless surface concentration

$\Gamma_n = \Gamma/\Gamma_c$ of rhamnilipids, respectively, and rewrite Eq. [S3]:

$$r_{net} = k(c_n - A{\Gamma_n}^2) \quad [S4]$$

The spatial-temporal dynamics of the bulk and the interface biosurfactant concentration c_n and Γ_n are described by the following coupled differential equations:

$$\frac{\partial c_n}{\partial t} = \nabla \cdot (D_c \nabla c_n) - k(c_n - A{\Gamma_n}^2) + \alpha_R \rho \frac{N}{K_N + N} \frac{B^m}{K_B^m + B^m} \quad [S5]$$

$$\frac{\partial \Gamma_n}{\partial t} = \nabla \cdot (D_\Gamma \nabla \Gamma_n) - \nabla \cdot [\eta_\Gamma \Gamma_n \nabla \gamma(\Gamma_n)] + k(c_n - A{\Gamma_n}^2) \quad [S6]$$

Here D_Γ, D_c, η_Γ, k, A, K_N, α_R, K_B, K_N, and m are constant parameters whose definitions and values are described in SI Table S2. Eq. [S5] describes the variation of c_n due to three processes, namely biosurfactant diffusion in the bulk phase, biosurfactant exchange between the liquid-air interface and the bulk phase (see Eq. [S4]), and biosurfactant production. The biosurfactant production term is proportional to bacterial density (ρ) and bacterial metabolic activity [which is limited by nutrient concentration N and modeled as a Hill function (Cao et al., 2016),$N/(K_N + N)$], and regulated by the QS activity (modeled as a Hill function of auto-inducer concentration B with Hill coefficient m (Cao et al., 2016)); ρ, N and B follow another set of differential equations to be described below. Eq. [S6] describes the variation of Γ_n due to biosurfactant diffusion at the interface, advective biosurfactant transport by Marangoni flows, as well as biosurfactant exchange between the liquid-air interface and the bulk phase. Biosurfactants adsorbed to the liquid-air interface will be carried by liquid flows in canals, hence giving rise to the advective transport term in Eq. [S6]. The speed of Marangoni flows in the advective transport term is proportional to surface tension gradient $\nabla\gamma(\Gamma_n)$ (de Gennes et al., 2003). Biosurfactant concentration in the bulk phase is assumed to be unaffected by Marangoni flows because the volume of the bulk phase is much greater than that of the canals in our experiments.

The spatial-temporal dynamics of N, ρ and B are described by the following coupled differential equations:

$$\frac{\partial N}{\partial t} = \nabla \cdot (D_N \nabla N) - \beta \frac{N}{K_N + N} \rho \qquad [S7]$$

$$\frac{\partial \rho}{\partial t} = \nabla \cdot (D_\rho \nabla \rho) - \nabla \cdot [\eta_\rho \rho \nabla \gamma(\Gamma_n)] + \beta \frac{N}{K_N + N} \rho \frac{1}{1 + \lambda \frac{B^m}{K_B^m + B^m}} \qquad [S8]$$

$$\frac{\partial B}{\partial t} = \nabla \cdot (D_B \nabla B) + \alpha_B \rho \frac{B^m}{K_B^m + B^m} + \chi \rho - d_B B \qquad [S9]$$

Here D_N, D_ρ, D_B, β, η_ρ, λ, α_B, χ, and d_B are constant parameters whose definitions and values are described in SI Table S2. The variation of the nutrient concentration field N (Eq. [S7]) is due to diffusion and consumption, with the nutrient consumption term being proportional to bacterial density ρ and bacterial metabolic activity $N/(K_N + N)$ as described above for Eq. [S5]. The variation of the bacterial density field ρ (Eq. [S8]) is due to three processes, namely diffusion, advective transport by Marangoni flows, and bacterial growth; the bacterial growth term is proportional to bacterial density ρ and bacterial metabolic activity, and is repressed by the QS-regulated biosurfactant production due to the associated metabolic cost. The variation of the QS auto-inducer concentration field B is described in Eq. [S9]. It includes 4 components, a diffusion term, a production term proportional to bacterial density ρ and regulated by QS activity via a Hill function with Hill coefficient m, a basal production term proportional to ρ (to ensure that autoinduction can be activated), and a degradation term.

Equations [S2, S5-S9] constitute the entire model for the spatial-temporal dynamics of biosurfactant distribution. All variables in the model are dimensionless. To simplify the computation we numerically solved Eqs. [S5-S9] in polar coordinate system with rotational symmetry. The computation was programmed in Fortran and complied by gFortran 9 on Linux platform. With appropriately chosen model parameters (SI Table S2), the magnitude of surface tension gradient was tuned to ~1000-3000 $\mathrm{mN \cdot m^{-2}}$, so as to match the estimated magnitude of surface tension gradient (Fig. 4A) required to generate the observed flow speed in canals (Fig. 3E).

SI Figures

Figure S1

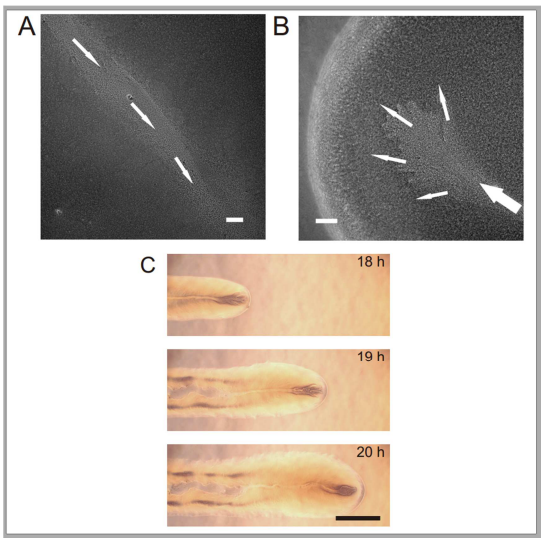

Fig. S1. Open channels supporting long-range directed material transport in *P. aeruginosa* colonies. (A) Phase-contrast microscopy image of an open channel in a *P. aeruginosa* (PA14 *flgK*::Tn5) colony. Arrows indicate the flow direction. Scale bar, 100 μm. Also see Movie S3. (B) Phase-contrast microscopy image taken near the tip of an open channel in a *P. aeruginosa* (PA14 *flgK*::Tn5) colony. Arrows indicate the flow direction. Scale bar, 100 μm. Also see Movie S4. (C) Image sequence taken by a DSLR camera via a 4X phase contrast objective lens showing the development of an open channel (or canal) in a branching colony of *P. aeruginosa* (PA14 *flgK*::Tn5). Scale bar, 1 mm. Also see Movie S6. The fluid flow in bacterial canals was sensitive to water content in the air environment and it was easily disrupted by decrease of humidity. Cells translocating along the open channels eventually settled in near the colony edge and they may contribute to colony expansion. Fluid flow in open channels on average went towards the colony edge and stopped abruptly at the very end (i.e. the tip) of an open channel, disappearing into the dense layer of cells near the edge (panel B; Movie S4).

Figure S2

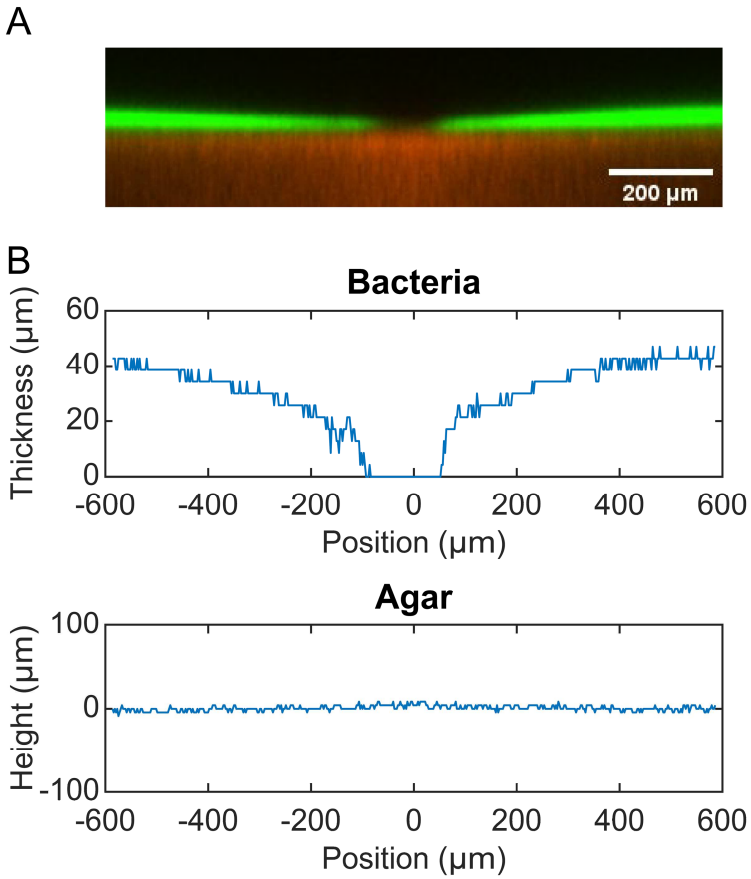

Fig. S2. Height profiles of colony and agar. (A) Cross-sectional view of the colony (green fluorescence) and the agar underneath the colony (red fluorescence) measured by laser scanning confocal microscopy (see Methods in main text). A canal is located at the center of the image. (B) Thickness profile of the colony (upper panel) and height profile the agar underneath the colony (lower panel) associated with panel A. The height of agar at position 600 □m was chosen as the reference level (i.e., height = 0 □m). The thickness of the colony is low inside the canal region due to flushing of fluid flows. The height of agar is uniform, showing that canal formation is not associated with agar degradation.

Figure S3

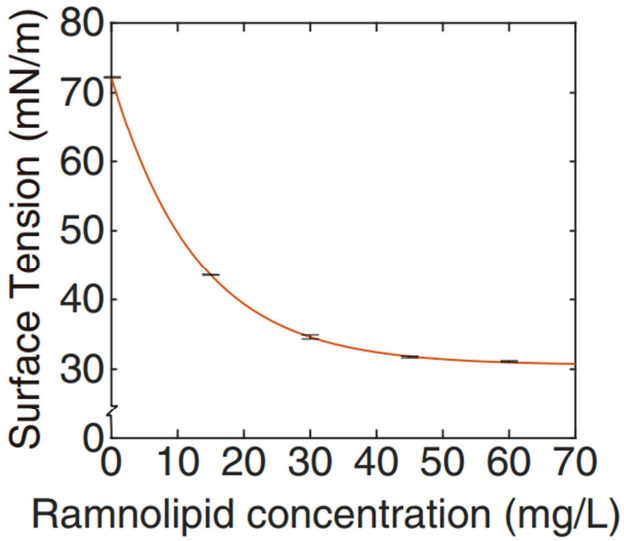

Fig. S3. Surface tension of rhamnolipid solutions as a function of rhamnolipid concentration. The relation between bulk rhamnolipid concentration and the steady-state surface tension. Steady-state surface tension was measured by pendant drop assay with a commercial contact-angle meter (OCA25, DataPhysics, Germany). The rhamnolipid solutions were prepared by dissolving rhamnolipids (in solid form) in M9DCAA medium. Error bars indicate the standard deviation. The line is a fit of data points to an exponential decay function (Eq. 1 of SI Text).

1414 Figure S4

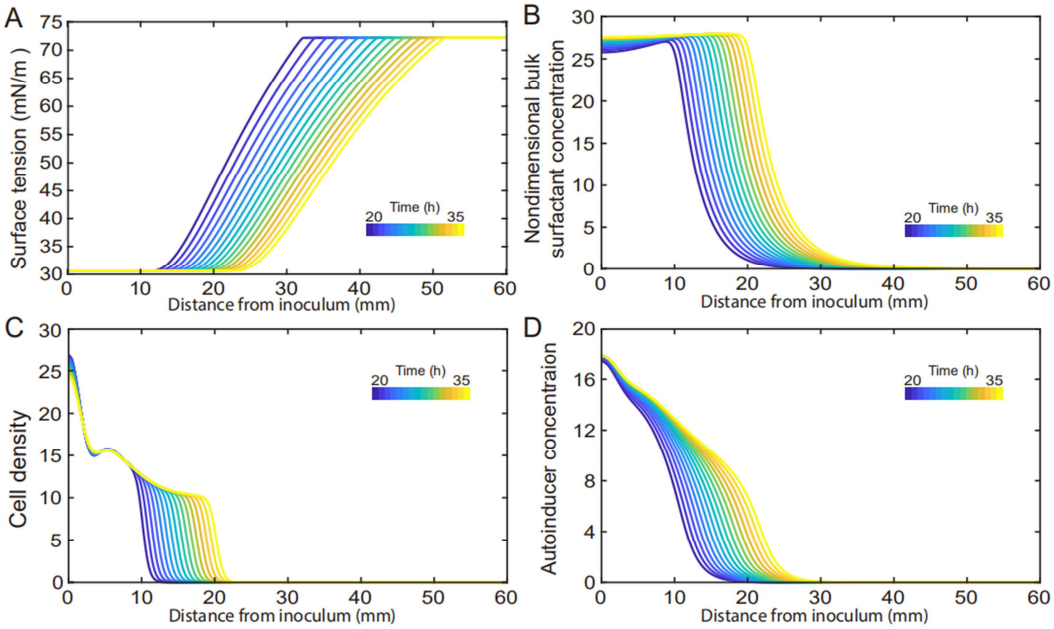

1415

1416 **Fig. S4. Spatial-temporal dynamics of key model variables related to the**
1417 **development of surface tension gradient in canals.** This figure is associated with
1418 main text Fig. 4. The spatial-temporal dynamics of the following variables used in the
1419 model presented in main text and SI were plotted: surface tension, panel (A); bulk
1420 biosurfactant concentration, panel (B); bacterial density, panel (C); autoinducer
1421 concentration, panel (D).

1422

1423

1424 Figure S5

1425

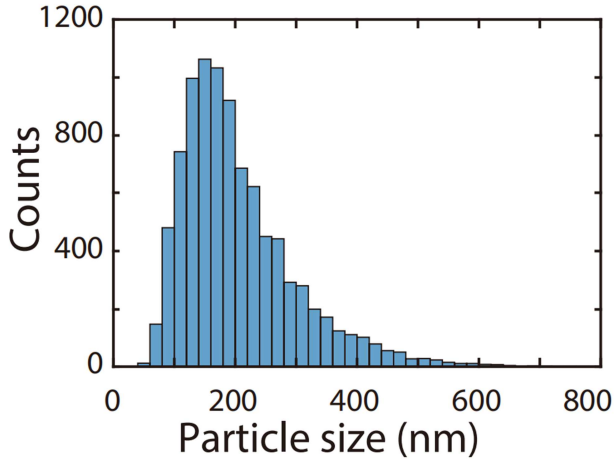

1426

1427 **Fig. S5. Size distribution of outer membrane vesicles (OMVs).** The OMVs were

1428 derived from canal-forming *P. aeruginosa* (PA14 *flgK*::Tn5) and the size distribution was

1429 measured by a particle sizer (NanoSight LM10, Malvern Instruments). See Methods.

Figure S6

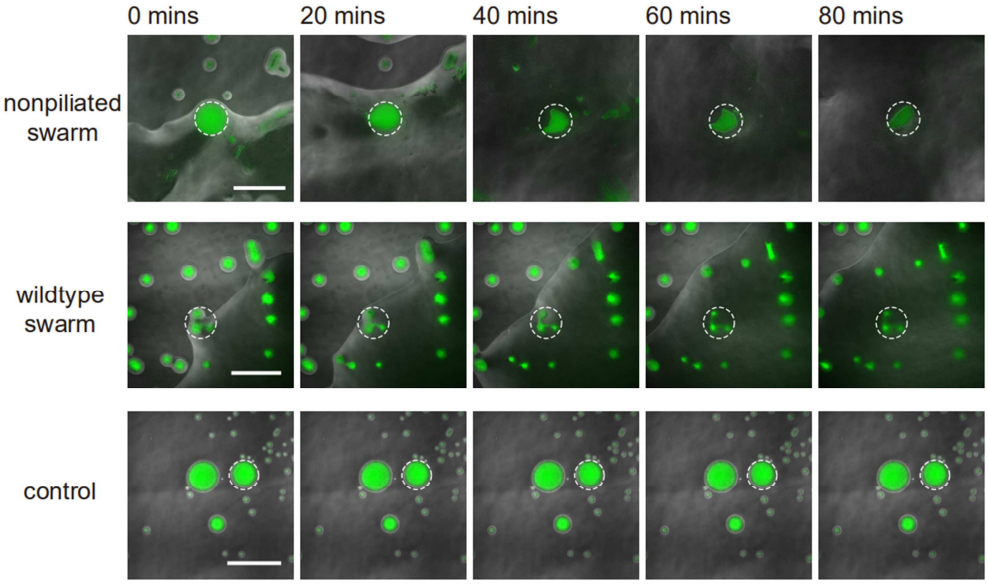

Fig. S6. Interaction between *S. aureus* and *P. aeruginosa* PA14 colonies. This figure is associated with Fig. 5, panels D,E. To compare with the effect of potential OMV transport due to flagellar motility, we co-cultured swarms of flagellated *P. aeruginosa* PA14 with *S. aureus* colonies under the same conditions as used in Fig. 5D. The image sequences show the temporal variation of *S. aureus* colony biomass (green fluorescence) under the following conditions: top, in contact with the swarming colony of PA14 Δ*pilB* mutant; middle, in contact with the swarming colony of wildtype PA14; bottom, control experiment in the absence of *P. aeruginosa*. Both PA14 Δ*pilB* mutant and wildtype PA14 have flagellar motility, but neither of them can form canals. In each panel the fluorescence image of *S. aureus* colonies (green) is superimposed onto the phase contrast image. The dashed circles mark the region with *S. aureus* colonies for fluorescence analysis in Fig. 5E. As shown in main text Fig. 5E, the *S. aureus* colonies encountering expanding *P. aeruginosa* swarms were destructed to a lesser extent compared to the case that were irrigated by canal flows, retaining ~20% and ~50% of cell mass after 60 min of contact with swarming colonies of *P. aeruginosa* PA14 Δ*pilB* mutant and wildtype PA14, respectively.

1453 Figure S7

1454

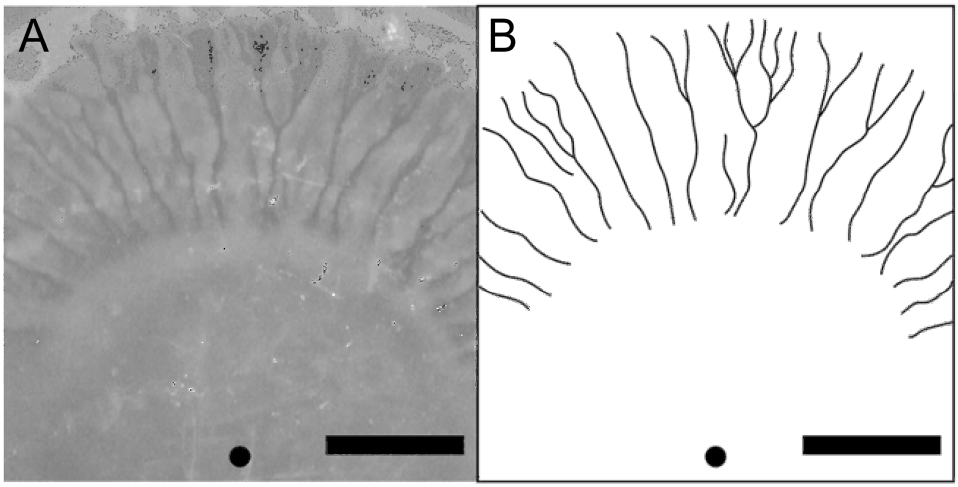

1455

1456

1457 **Fig. S7. Canal formation in *Serratia marcescens* colonies.** Overnight culture of *S.*
1458 *marcescens* grown in LB medium was inoculated on 0.6% Eiken agar plates and
1459 photographed in a custom-built imaging incubator made of PMMA. The temperature of
1460 the incubator was maintained at 30 °C and the images of canals were photographed by
1461 a digital single-lens reflex camera. (A) Canal appeared ~4 h after colony inoculation.
1462 (B) Sketch of the canals in panel A for better visualization. The black dot represents the
1463 inoculum. Scale bars, 500 μm.

1464

Figure S8

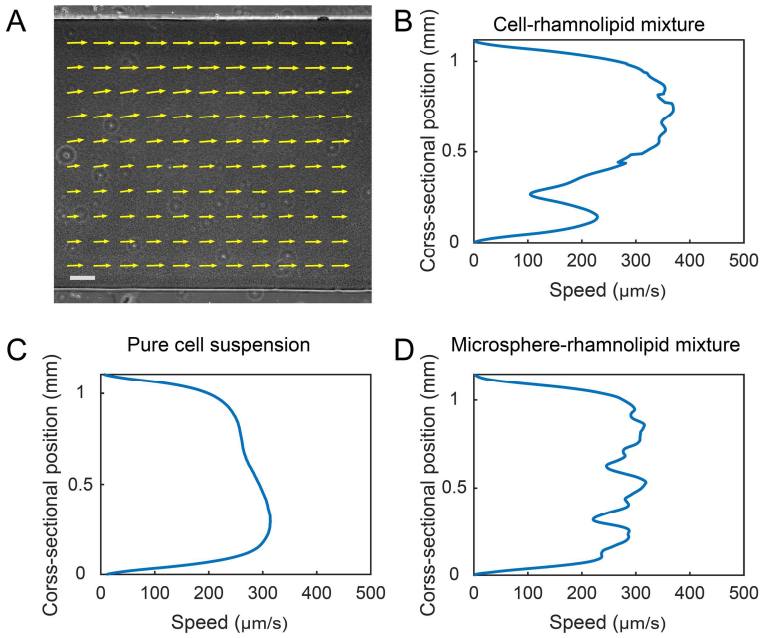

Fig. S8. Shear banding of cell-rhamnolipid mixture in PDMS microfluidic channels. (A) Flow velocity field of cell-rhamnolipid mixture in a microfluidic channel. The microfluidic channel had a rectangular cross-section (200 μm of height, 1.1 mm of width). Cells (PA14 *flgK*::Tn5; ZK3367) and rhamnolipids were mixed at a final density (concentration) of $1.9X10^{10}$ cells/mL and 10 mg/mL, respectively, and driven by a syringe pump at a flow rate of 5 □L/min. The velocity field was measured by PIV analysis on phase-contrast image sequence and averaged over a time window of 5 s. The velocity field is superimposed onto one of the analyzed phase-contrast images. Arrows indicate velocity vectors. Scale bar, 100 □m. (B) Cross-sectional flow speed profile computed based on velocity field data shown in panel A. Each data point represents local velocity averaged in a domain of 41.6um x 41.6um centered around the cross-sectional position. (C,D) Cross-sectional flow speed profile in microfluidic channels filled with other fluids. Data in panel C was obtained with pure cell suspension ($1.9X10^{10}$ cells/mL), and data in panel D with a mixture of rhamnolipids (10 mg/mL) and 1.1-□m microsphere suspension (~$1.9x10^{10}$ particles/mL). These fluids were driven through microfluidic channels by a syringe pump at a flow rate of 3 □L/min. The flow speed profiles were computed based on the respective time-averaged velocity field, which was obtained by PIV analysis on phase-contrast image sequence and averaged over a time window of 5 s. Each data

point in C,D represents local velocity averaged in a domain of 41.6um x 41.6um centered around the cross-sectional position. See Methods for details of experiments and image analysis associated with all panels.

Figure S9

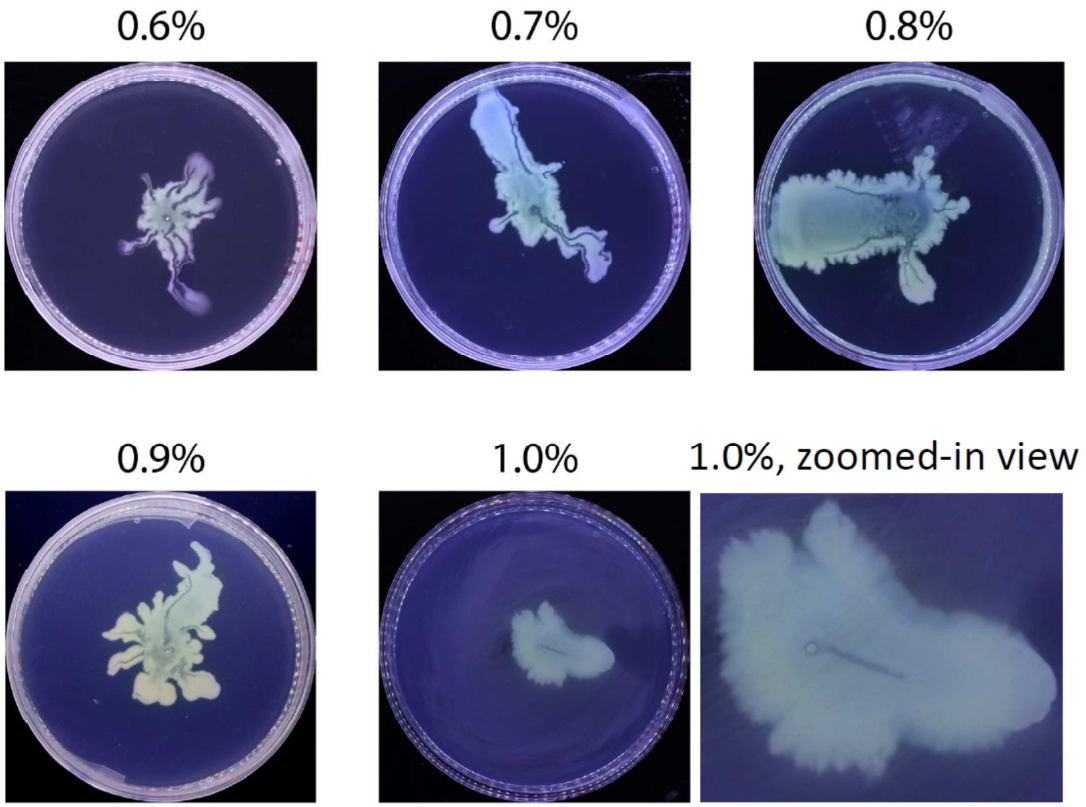

Fig. S9. Representative images of canal development at different agar concentrations. The colonies were from the same batch and incubated under the same condition (30 ºC) for the following durations: 0.6%-0.8%, 19 hr; 0.9%, 24 hr; 1.0%, 36 hr. Canals can be found in different agar (infused with M9DCAA medium) concentrations from 0.6% to 1.0%, in addition to the 0.5% agar used in the main text. Note that a canal in the colony on the 1.0% plate is located at the center (see the zoomed-in view).

SI Tables

Table S1. Primers

No.	Oligo Name	Sequence 5' to 3'
1	1-rhlA_UpF	agctcggtacccgggGGGTGATTTCCTACGGGGTG
2	2-rhlA_UpR	CTTCGCAGGTCAAGGGTTCACCGCATTTCACACCTCCCAA
3	3-rhlA_DownF	TTGGGAGGTGTGAAATGCGGTGAACCCTTGACCTGCGAAG
4	4-rhlA_DownR	cgacggccagtgccaCCGTACTTCTCGTGAGCGAT
5	rhlA_F	GACAAGTGGATTCGCCGCA
6	rhlA_R	TTGAACTTGGGGTGTACCGG
7	rhlAGENE_F	GGTCAATCACCTGGTCTCCG
8	rhlAGENE_R	GCTGATGGTTGCTGGCTTTC
9	Pk18-F	TGCTTCCGGCTCGTATGTTG
10	Pk18-R	GCGAAAGGGGGATGTGCTG

Table S2. Simulation parameters

Parameter	Description	Value	Unit	Robust range #
α_R	Biosurfactant synthesis rate	2×10^{-3}	s^{-1}	5×10^{-4} - 1×10^{-2}
β	Bacterial growth rate	6×10^{-4}	s^{-1}	3×10^{-4} - 1×10^{-3}
K_N	Nutrient concentration for half maximal metabolic activity	1	Nondimensio-nal	N/A
K_B	Half-activation threshold of QS auto-inducer	1	Nondimensio-nal	N/A
α_B	Auto-inducer	2×10^{-4}	s^{-1}	1×10^{-4} - 1×10^{-3}

	synthesis rate			
d_B	Auto-inducer degradation rate	2×10^{-4}	s^{-1}	0 - 2×10^{-4}
χ	Auto-inducer basal production rate	2×10^{-6}	s^{-1}	1×10^{-6} - 2×10^{-5}
m *	Hill coefficient of QS regulation	2		N/A
λ	Parameter of growth-repression due to QS-regulated biosurfactant production	0.3	Nondimensio-nal	0-0.5
k **	Reaction rate constant for biosurfactant transfer between the bulk phase and the interface	2×10^{-5}	s^{-1}	N/A
A ***	Ratio between bulk surfactant concentration and square of the steady-state surface density	6.125	Nondimensio-nal	2-10
η_ρ **	Parameter of advective bacterial transport	5×10^{-11}	$(mN\bullet m^{-2})^{-1}s^{-1}$	N/A
η_Γ **	Parameter of advective biosurfactant transport	2.5×10^{-10}	$(mN\bullet m^{-2})^{-1}s^{-1}$	N/A
D_c	Diffusion coefficient of biosurfactant in	1×10^{-9}	m^2s^{-1}	0 - 1×10^{-9}

	bulk phase			
D_Γ	Diffusion coefficient of biosurfactant at liquid-air interface	5×10^{-11}	m^2s^{-1}	$0 - 1\times10^{-10}$
D_ρ	Diffusion coefficient of bacteria	5×10^{-11}	m^2s^{-1}	$0 - 5\times10^{-11}$
D_B	Diffusion coefficient of auto-inducers	1×10^{-9}	m^2s^{-1}	$5\times10^{-10} - 1\times10^{-9}$
D_N	Diffusion coefficient of nutrient	1×10^{-9}	m^2s^{-1}	$0 - 2\times10^{-9}$

The results shown in main text Fig. 4D,E are robust to variation of parameters within the indicated range.

* The value of this parameter is taken from reference (Payne et al., 2013).

** These parameters are chosen to yield the width of the plateau of surface tension gradient distribution (Fig. 4D) being ~25 mm (matching the experimental results).

*** The value of this parameter is taken from reference (Hanyak et al., 2012).

Legends of SI Movies

Movie S1. Rapid cellular flow streaming through a nonpiliated *P. aeruginosa* (PA14 Δ*pilB*) colony. Cells are motile outside the stream.

Movie S2. Cellular flow in an open channel of non-motile *P. aeruginosa* (PA14 *flgK*::Tn5 Δ*pilA*) colony. This real-time video is associated with Fig. 1E in main text.

Movie S3. Cellular flow in an open channel of a piliated *P. aeruginosa* (PA14 *flgK*::Tn5) colony. This real-time video is associated with Fig. S1, panel A.

Movie S4. Cellular flow near the tip of an open channel in a piliated *P. aeruginosa* (PA14 *flgK*::Tn5) colony. The flow slowed down and stopped abruptly at the tip, disappearing into the dense layer of cells near the edge of the colony. Note that the colony edge had ceased expansion and in general, canal formation does not necessarily coincide with colony expansion. This real-time video is associated with Fig. S1, panel B.

Movie S5. Development of open channels in branching colonies of piliated *P. aeruginosa* (PA14 *flgK*::Tn5). The colony was grown on M9DCAA agar plates at 30 ºC. Time label shows the elapsed time from inoculation (hh:mm). The video is associated with Fig. 1F in main text.

Movie S6. Zoomed-in view of a developing bacterial canal in a branching colony of

piliated *P. aeruginosa* (PA14 *flgK*::Tn5). Time label shows the elapsed time from inoculation (hh:mm). The video is associated with Fig. S1, panel C.

Movie S7. Effect of externally applied counteracting surface tension gradient on fluid transport in canals. An agar patch infused with surfactant TWEEN 20 (50 mg/mL) was placed at ~1 cm in front of a colony branch of piliated *P. aeruginosa* (PA14 *flgK*::Tn5); see Methods. As shown in the video, immediately following this operation, fluid flows in the canal gradually ceased and the canal slowly retracted. Time label shows the elapsed time from placing the agar patch (mm:ss).

Movie S8. Distinct flow regimes occurring in a homogeneous region of a piliated *P. aeruginosa* (PA14 *flgK::Tn5*) colony. The video is associated with Fig. 3A,B in main text.

Movie S9. The course of a developing canal in a colony. Cells in the colony hosted a plasmid expressing the rhamnolipid synthesis reporter P_{rhlA}-*gfp*(*ASV*) and the colony was imaged by fluorescence microscopy. Scale bar, 125 μm. Time label is in the format of hh:mm:ss. The video is associated with Fig. 3C in main text.

Movie S10. Transport of outer membrane vesicles (OMVs) along a canal. This real time video records at 10 frames per second the fluorescence of FM1-43 FX labeled OMVs that were being transported along a canal in a *P. aeruginosa* (PA14 *flgK*::Tn5) colony. Purified OMVs was injected into the canal at ~15 mm upstream from the tip of the canal, and the video was acquired after ~2 min at ~5 mm upstream from the tip of the canal. The video is associated with Fig. 5C in main text.

Movie S11. Eradication of an *S. aureus* colony irrigated by *P. aeruginosa* canal flows. *S. aureus* (with constitutive GFP expression) colonies were co-cultured with *P. aeruginosa* (PA14 *flgK*::Tn5); see Methods. Time label (in hh:mm format) shows the elapsed time from full contact between the *P. aeruginosa* colony and the *S. aureus* colony near the center. The fluorescence image of *S. aureus* colonies is displayed in logarithmically transformed pixel values, in order to accommodate the broad dynamic range. In each video frame the fluorescence image is superimposed onto the corresponding phase contrast image acquired simultaneously. As shown in the video, the *S. aureus* colony irrigated by *P. aeruginosa* canal flows was quickly eradicated, while a nearby *S. aureus* colony that came into full contact with the *P. aeruginosa* colony but did not encounter canal flows retained ~40% colony biomass after ~60 min. The video is associated with Fig. 5D in main text.